

2

NAVAL POSTGRADUATE SCHOOL

Monterey, California

AD-A243 794



DTIC
ELECTE
DEC 31 1991
S D

THESIS

A NUMERICAL STUDY OF THE EFFECTS
OF WIND FORCING ON THE CHILEAN CURRENT
SYSTEM

by

Jeffrey L. Bacon

March 1991

Thesis Advisor

Mary L. Batteen

Approved for public release; distribution is unlimited.

Prepared for:
Office of Naval Research
800 N. Quincy Street
Arlington, VA 22217-5000

91-19138



01 1227 010

NAVAL POSTGRADUATE SCHOOL
Monterey, California

Rear Admiral R. W. West
Superintendent

Provost H. Shull

The work reported herein was supported by and prepared for the U.S.
Office of Naval Research, Arlington, Virginia.

Reproduction of all or part of this report is authorized.

Principal author for this report was

J. L. Bacon
J. L. Bacon, LCDR, USN

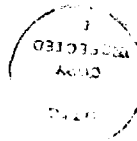
Approved by:

C. A. Collins
C. A. Collins, Chairman
Department of Oceanography

Released by:

P. J. Marfo
P. J. Marfo, Dean of Research

Accession For	
NTIS CRA&I	↓
DTIC TAB	
Unannounced	
Justification	
By	
Distribution/	
Availability Codes	
Dist	Availability Codes Special
A-1	



REPORT DOCUMENTATION PAGE

1a. REPORT SECURITY CLASSIFICATION UNCLASSIFIED			1b. RESTRICTIVE MARKINGS	
2a. SECURITY CLASSIFICATION AUTHORITY			3. DISTRIBUTION / AVAILABILITY OF REPORT	
2b. DECLASSIFICATION / DOWNGRADING SCHEDULE			Approved for public release. Distribution is unlimited.	
4. PERFORMING ORGANIZATION REPORT NUMBER(S) NPS OC-91-001			5. MONITORING ORGANIZATION REPORT NUMBER(S)	
6a. NAME OF PERFORMING ORGANIZATION Naval Postgraduate School		6b. OFFICE SYMBOL (If applicable) OC		7a. NAME OF MONITORING ORGANIZATION Office of Naval Research
6c. ADDRESS (City, State, and ZIP Code) Monterey, California 93943-5000			7b. ADDRESS (City, State, and ZIP Code) 800 N. Quincy Street Arlington, VA 22217-5000	
8a. NAME OF FUNDING / SPONSORING ORGANIZATION Naval Postgraduate School		8b. OFFICE SYMBOL (If applicable) OC		9. PROCUREMENT INSTRUMENT IDENTIFICATION NUMBER O&MN, Direct Funding
8c. ADDRESS (City, State, and ZIP Code) Monterey, California 93943-5000			10. SOURCE OF FUNDING NUMBERS	
			PROGRAM ELEMENT NO.	PROJECT NO.
			TASK NO.	WORK UNIT ACCESSION NO.
11. TITLE (Include Security Classification) A NUMERICAL STUDY OF THE EFFECTS OF WIND FORCING ON THE CHILEAN CURRENT SYSTEM				
12. PERSONAL AUTHOR(S) Bacon, Jeffrey L. in conjunction with M.L. Batteen and C.S. Nelson				
13a. TYPE OF REPORT Master's Thesis		13b. TIME COVERED FROM _____ TO _____		14. DATE OF REPORT (Year, Month, Day) March 1991
15. PAGE COUNT 79				
16. Supplementary Notation The views expressed in this thesis are those of the author and do not reflect the official policy or position of the Department of Defense or the U.S. Government.				
17. COSATI CODES			18. SUBJECT TERMS (Continue on reverse if necessary and identify by block number)	
FIELD	GROUP	SUB-GROUP	eastern boundary current, eddies, wind forcing, Chile Current	
19. ABSTRACT (Continue on reverse if necessary and identify by block number)				
<p>A high-resolution, multi-level, primitive equation ocean model is used to examine the response of an idealized, flat-bottomed, eastern boundary oceanic regime on a beta-plane to both steady and daily-varying climatological wind forcing. The area of study is a coastal region within the Chile Current System from 22° S to 34° S. When steady wind forcing is used, an equatorward surface current and poleward flowing undercurrent develop. Eddies are also generated, with initial formation in the poleward end of the domain. When daily-varying wind forcing is used, there is large spatial variability in the oceanic response. A relatively weak poleward flowing undercurrent appears, first in the poleward part of the domain. An equatorward surface current also develops and intensifies during the upwelling season. Eddies are generated and develop farther poleward in the domain than in the first experiment. The eddies are largest in the equatorward end of the domain. The eddy motion is closely tied to seasonal influences, with cyclonic (divergent) eddies traversing towards areas of higher dynamic heights when there are divergent wind fields present, and vice versa. In addition to the currents and eddies, upwelling and cold filaments are evident in both experiments.</p>				
20. DISTRIBUTION / AVAILABILITY OF ABSTRACT <input checked="" type="checkbox"/> UNCLASSIFIED/UNLIMITED <input type="checkbox"/> SAME AS RPT <input type="checkbox"/> DTIC USERS			21. ABSTRACT SECURITY CLASSIFICATION Unclassified	
22a. NAME OF RESPONSIBLE INDIVIDUAL M.L. Batteen			22b. TELEPHONE (Include Area Code) (408) 646-2768	22c. OFFICE SYMBOL OC/Bv

Approved for public release; distribution is unlimited.

A Numerical Study of the Effects
of Wind Forcing on the Chilean Current System

by

Jeffrey L. Bacon
Lieutenant Commander, United States Navy
B.A., University of New Mexico, 1979

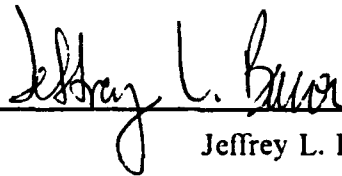
Submitted in partial fulfillment of the
requirements for the degree of

MASTER OF SCIENCE IN METEOROLOGY AND PHYSICAL
OCEANOGRAPHY

from the

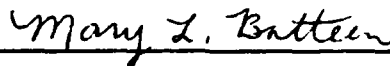
NAVAL POSTGRADUATE SCHOOL
March 1991

Author:

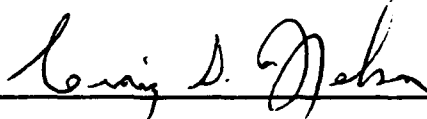


Jeffrey L. Bacon

Approved by:



Mary L. Batteen, Thesis Advisor



Craig S. Nelson, Second Reader



Curtis A. Collins, Chairman,
Department of Oceanography

ABSTRACT

A high-resolution, multi-level, primitive equation ocean model is used to examine the response of an idealized, flat-bottomed, eastern boundary oceanic regime on a beta-plane to both steady and daily-varying climatological wind forcing. The area of study is a coastal region within the Chile Current System from 22° S to 34° S. When steady wind forcing is used, an equatorward surface current and poleward flowing undercurrent develop. Eddies are also generated, with initial formation in the poleward end of the domain. When daily-varying wind forcing is used, there is large spatial variability in the oceanic response. A relatively weak poleward flowing undercurrent appears, first in the poleward part of the domain. An equatorward surface current also develops and intensifies during the upwelling season. Eddies are generated and develop farther poleward in the domain than in the first experiment. The eddies are largest in the equatorward end of the domain. The eddy motion is closely tied to seasonal influences, with cyclonic (divergent) eddies traversing towards areas of higher dynamic heights when there are divergent wind fields present, and vice versa. In addition to the currents and eddies, upwelling and cold filaments are evident in both experiments.

TABLE OF CONTENTS

I. INTRODUCTION	1
II. BACKGROUND	2
A. REGIONAL DESCRIPTION	2
1. Surface current	2
2. Peru-Chile Undercurrent	3
B. CLIMATOLOGICAL WINDS	4
III. MODEL DESCRIPTION	6
A. MODEL EQUATIONS	6
B. MODEL DOMAIN AND RESOLUTION	7
C. FINITE DIFFERENCE SCHEME	9
D. HEAT AND MOMENTUM DIFFUSION	9
E. SURFACE THERMAL FORCING	9
F. BOUNDARY CONDITIONS	10
G. INITIAL CONDITIONS	12
H. EXPERIMENTAL CONDITIONS	13
1. Experiment One: Constant Wind Stress	13
2. Experiment Two: Variable Climatological Winds	13
IV. ANALYSIS TECHNIQUES	21
A. ENERGY ANALYSIS	21
B. SPECTRAL ANALYSIS	23
V. RESULTS OF THE WIND FORCING EXPERIMENTS	24
A. EXPERIMENT 1	24
B. EXPERIMENT 2	26
VI. SUMMARY AND RECOMMENDATIONS	57
A. SUMMARY	57
B. RECOMMENDATIONS	58

BIBLIOGRAPHY	61
--------------------	----

INITIAL DISTRIBUTION LIST	66
---------------------------------	----

LIST OF TABLES

Table 1. VALUES OF CONSTANTS USED IN THE MODEL	8
Table 2. VARIABLES USED IN COMPUTING NET HEAT FLUX	11

LIST OF FIGURES

Figure 1.	Surface current and undercurrent, from Silva and Fonseca (1983)	5
Figure 2.	Model Domain	16
Figure 3.	Temperature profile used in both experiments	17
Figure 4.	Wind stress fields from Bakun and Nelson (1991)	18
Figure 5.	Wind stress curl fields from Bakun and Nelson (1991)	19
Figure 6.	Wind speed vectors with magnitude contours	20
Figure 7.	Surface current vectors, temperature, meridional velocity and dynamic height at day 50 of Experiment 1	30
Figure 8.	U (surface zonal velocity) for Experiment 1	31
Figure 9.	Baroclinic and barotropic instability at day 50 of Experiment 1.	32
Figure 10.	Surface current vectors, temperature, meridional velocity and dynamic height at day 60 of Experiment 1	33
Figure 11.	Spectral density at day 60 of Experiment 1	34
Figure 12.	Zonal cross-sections of north-south velocity (V) at day 60 of Experiment 1	35
Figure 13.	Surface current vectors, temperature, meridional velocity and dynamic height at day 120 of Experiment 1	36
Figure 14.	Baroclinic and barotropic instability at day 120 of Experiment 1.	37
Figure 15.	Zonal cross-sections of north-south velocity (V) at day 120 of Experiment 1	38
Figure 16.	Surface current vectors, temperature, meridional velocity and dynamic height at day 160 of Experiment 1	39
Figure 17.	Zonal cross-sections of north-south velocity (V) at day 160 of Experiment 1	40
Figure 18.	Spectral density at day 160 of Experiment 1	41
Figure 19.	Zonal cross-sections of north-south velocity (V) at day 160 of Experiment 1	42
Figure 20.	Surface current vectors, temperature, meridional velocity and dynamic height at day 210 of Experiment 1	43
Figure 21.	Zonal cross-sections of north-south velocity (V) at day 40 of Experiment 2	44

Figure 22. Zonal cross-sections of north-south temperature (T) at day 50	45
Figure 23. Surface current vectors, temperature, zonal velocity and dynamic height at day 50 of Experiment 2	46
Figure 24. Surface zonal velocity (U) for Experiment 2	47
Figure 25. Spectral Density at day 80 of Experiment 2	48
Figure 26. Zonal cross-sections of north-south velocity (V) at day 80 of Experiment 2	49
Figure 27. Dynamic height, days 80-140 of Experiment 2	50
Figure 28. Baroclinic and barotropic instability at day 140 of Experiment 2.	51
Figure 29. Surface temperature contours for Experiment 2	52
Figure 30. Zonal cross-sections of north-south velocity (V) at day 250 of Experiment 2	53
Figure 31. Spectral density at day 250 of Experiment 2	54
Figure 32. Dynamic height, days 250-280 of Experiment 2	55
Figure 33. Dynamic height, days 290-350 of Experiment 2	56
Figure 34. Temperature contours from (A) satellite and (B) model output	60

ACKNOWLEDGMENTS

The author wishes to thank Dr. Mary Batteen for her guidance and patience, and especially for her dedication to the science of oceanography. Thanks also to Dr. Collins for his encouragement, and CDR Nelson for his thoughtful assistance (not to mention the use of his wind data). Special thanks to Bob, Arlene, and Pedro, who were nothing less than incredible in their computer and geological skills. Finally, thank you Rebecca, for your love, companionship, and belief in me when I had my doubts.

I. INTRODUCTION

The eastern boundary current system adjacent to the west coast of Chile, although well known for its biological productivity, has (until recently) attracted relatively little investigation into the physical oceanography of the region, despite an obvious relationship between the fertile waters in the region, and the fluid dynamics that make them so. The mean climatological current system is comprised of several major features, including: the equatorward flowing surface current called the Chile-Peru Current, and a poleward flowing countercurrent and/or undercurrent known as both the Gunther Current and the Peru-Chile Undercurrent.

Eddies, jets and other instabilities that form along this and other eastern boundary current systems (e.g., the California Current System) have begun to generate a significant amount of interest. Process-oriented studies using numerical models, such as those spearheaded by Batteen *et al.* (1989), attempt to quantify the forces that create these features.

Because the Chile Current System has not been previously investigated with numerical models, the objective of this thesis will be to investigate the effects that wind forcing has on the generation of currents, eddies and filaments in the Chile Current system. A high-resolution, multi-level, primitive equation model will be used to simulate the effects of wind stress on the eastern boundary current region off Chile. The numerical model used for this study is one developed by Haney (1985), and adapted for eastern boundary current regions by Batteen (1989).

The study is organized as follows. In Chapter II we review the oceanic and wind regime off the coast of Chile. In Chapter III we discuss the numerical model used, as well as the specific initial and experimental conditions. In Chapter IV we describe the analysis techniques used to investigate the dynamical reasons for eddy generation. The modeling results are presented in Chapter V, and a summary is given in Chapter VI.

II. BACKGROUND

A. REGIONAL DESCRIPTION

1. Surface current

The mean climatological ocean adjacent to the coast of Chile is an eastern boundary current regime that consists of a slow-moving (~ 10 cm/s) surface current overlying a relatively strong (~ 25 cm/s) and steady coastal undercurrent (Wooster and Reid, 1963). The surface current is similar to other eastern boundary currents in that it is a sluggish, wide and generally shallow stream moving equatorward along a west coast (Wooster and Reid, 1963). Mass transports have been estimated to be between 17.4×10^6 - 19.0×10^6 m/s (Wooster and Reid, 1963). The primary source of the Chile-Peru Current is, as expected, the West Wind Drift, because the South American continent extends far enough south to intercept at least part of the flow, and divert it towards the north. Because the high latitudes are areas where precipitation typically exceeds evaporation, the northward flowing waters are relatively low in salinity, averaging less than 34.5 ppt. As the flow moves towards the north, salinity levels increase because of mixing and the general increase in evaporation along the way (Wooster and Reid, 1963).

Tchernia (1980) and Gunther (1936) characterize the Chile Current System as consisting of two equatorward flowing currents, separated by a seasonal surface countercurrent. The outer current is usually referred to by those who adhere to this "two current" philosophy as the Oceanic Chile-Peru Current; it extends to depths of never more than 1000 m (Wooster and Reid, 1963), and usually no more than 700 m (Tchernia 1980). The inner surface current is known as the Coastal Chile-Peru Current, with a maximum depth of ~ 200 m (Tchernia, 1980).

Another description of the Chile-Peru Current is that it is a single, broad, slow, and sometimes intermittent surface current overlying a poleward flowing undercurrent (see Fonseca, 1989). In addition, Wooster and Reid (1963) describe the Chile-Peru Current as the principal component of the meridional circulation in the South Pacific.

Yet another view of the Chile Current System is a combination of the previous discussions. Fonseca (1989) describes the current as being primarily one body of water; however, he states that in the southern domain the current is physically split into two components, due to either a countercurrent as described by Tchernia (1980), or to an undercurrent that has broached the surface (discussed in the next section).

2. Peru-Chile Undercurrent

Beneath the surface flow is a steady, poleward undercurrent, generally known as the Peru-Chile Undercurrent (PCU). The undercurrent is strong and steady enough to be considered by some (e.g., Fonseca, 1989) to be the dominant ocean circulation feature in the Chilean eastern boundary current region, often broaching the surface of the ocean in spite of predominantly equatorward winds throughout the year. Figure 1, from Silva and Fonseca (1983), illustrates the relationship between the surface current and undercurrent at different times of the year. The PCU is overlain by an equatorward surface current south of 30°S, but broaches the surface and widens north of 30°S. The PCU is wider and more of a dominant feature in the north during the summer months, and becomes narrower during the winter. In the south, the PCU is dominated by the surface current, especially in the summer months, when winds are more meridional in orientation. Tchernia (1980) also acknowledges the existence of an undercurrent, describing it as distinct and flowing beneath the countercurrent, with depths extending to several hundred meters.

Until recently, the PCU had been relatively unexplored. Gunther (1936) discussed the undercurrent that would eventually carry his name, but very little additional research was conducted on the PCU until 1961, when Wooster and Gilmartin (1961) measured it using parachute drogues. Their article sparked a new interest in the region, and soon several expeditions set out to study the waters adjacent to the South American coast. Between 1960 and 1982 the area was explored by twelve different expeditions (Fonseca, 1989). Results of the experiments revealed some consistent traits of the PCU:

1. The PCU is present all year.
2. It is easily distinguishable from the surface to about 600 *m* depth.
3. Its core is at approximately 150-200 *m* depth.
4. It is principally located between the coast and 200 *km* offshore.
5. Average speeds are on the order of 25 *cm/s*.
6. Transport is estimated to be $10 \times 10^6 \text{ m}^3/\text{s}$.

In a recent workshop on poleward flows along eastern ocean boundaries, Clarke (1989) concluded that, although many mechanisms may cause mean flows along eastern boundary regions, only two have thus far been shown to have a significant impact on the creation of a poleward flowing undercurrent. The first of these is the generation of poleward flow by small-scale irregularities on the ocean bottom, in which coastally trapped lee waves are formed by the irregularities under the influence of a mean

equatorward flow. Poleward flows of this type were estimated by Clarke (1989) to be of such a small magnitude (~ 2.5 cm/s) that we will neglect them in this study. The other mechanism mentioned by Clark (1989) that can generate poleward flows of significant magnitudes (~ 25 cm/s) is wind stress, the role of which will be studied in this paper.

B. CLIMATOLOGICAL WINDS

The Chile Current System is influenced predominantly by equatorward winds throughout the year. The direction, and to a large degree the magnitude of the winds are the result of a semi-permanent subtropical high pressure system that is similar in nature and behavior to its counterpart in the Northern Hemisphere, the North Pacific Subtropical High, as described in Nelson (1977).

The South Pacific Subtropical High migrates meridionally with the seasons, reaching its northernmost extent during the austral winter, with its center located roughly at 20°S . As the seasons progress, the high pressure system moves southward until its center reaches about 30°S during the summer months.

Because of this migration, maximum values of wind stress and wind stress curl vary temporally at given locations. In Peru, for example, the maximum wind stress and wind stress curl values are seen during the austral winter months (Bakun and Nelson, 1991), presumably because the South Pacific Subtropical High reaches its northernmost migration at that time, and the resulting winds take on more of an alongshore characteristic. The middle of the Chilean coastline, in contrast, does not experience maximum wind stress and wind stress curl values until late spring and summer, corresponding to the upwelling season in that region (Fonseca, 1989). Maximum wind stress curl values for the entire region are seen during the austral summer months, near 33°S .

Winds stress curl values are usually at a relative minimum in the region off the northwest coast of Chile, compared to the rest of the Chilean coastal waters. Bakun and Nelson (1991) argue that this curl minima (i.e., anticyclonic curl) might be caused by the coastal winds blowing into the coastal bend near Arica, rather than remaining parallel to the coast. As the winds blow onto the land, alongshore speeds would in effect go to zero, eliminating any wind stress curl-induced upwelling. Wooster (1970) discusses a cyclonic curl minimum in the same area, although he concentrates on the curl of the surface current, rather than on that of the wind. His discussion does, however, tend to support the observation that cyclonic curl values are at a relative minimum near Arica.

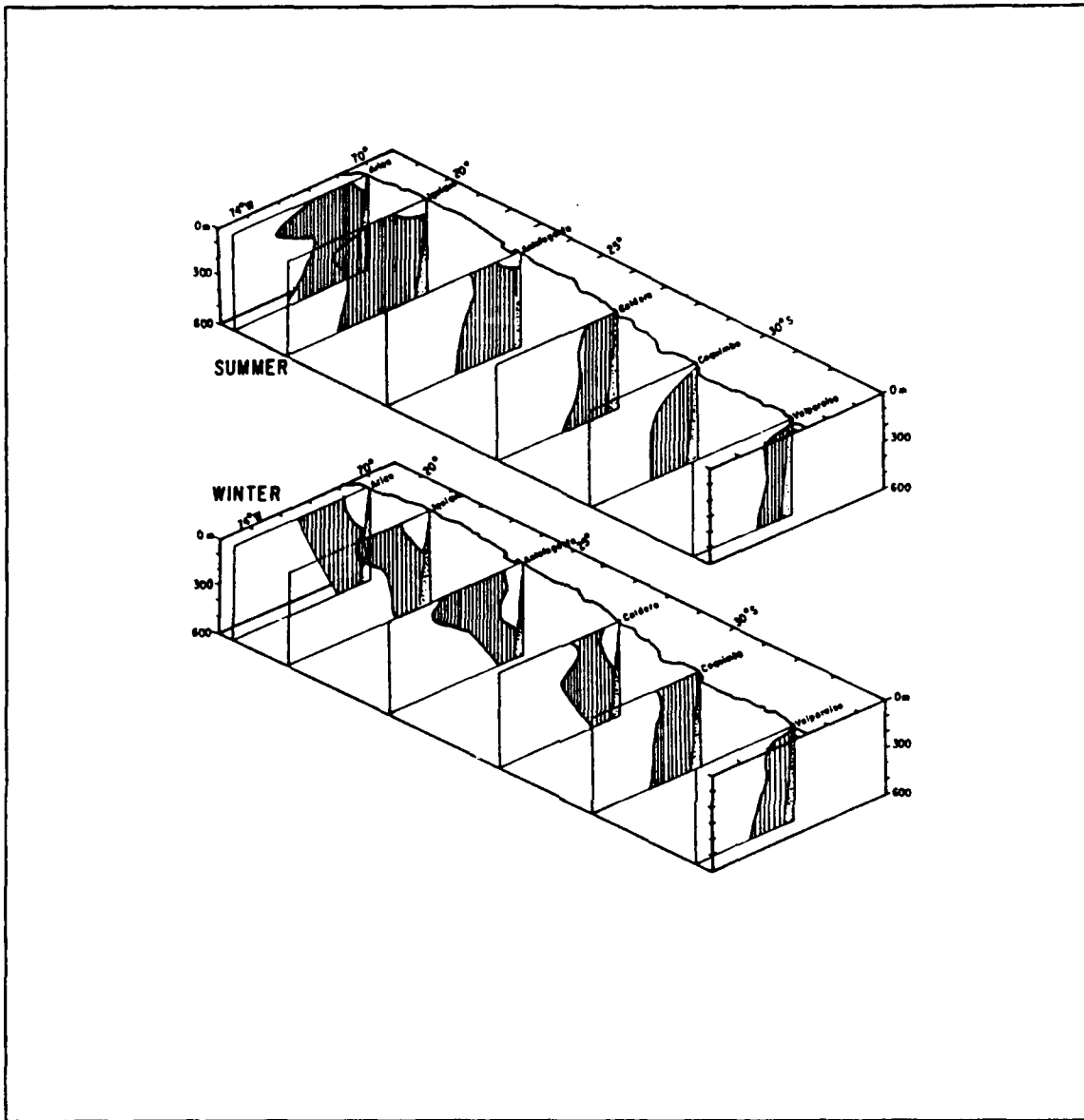


Figure 1. Surface current and undercurrent, from Silva and Fonseca (1983): Simplified representation of the Peru-Chile Undercurrent (shaded) between the coast of Chile and ~ 290 km offshore.

III. MODEL DESCRIPTION

A. MODEL EQUATIONS

The numerical model used in this study was originally developed by Haney (1985), and later adapted by Batteen *et al.* (1989) for application to eastern boundary current regions. The following description of the model equations is based primarily on similar descriptions found in those papers. The multi-level, primitive equation (PE) model uses the hydrostatic, rigid lid, β -plane, and Boussinesq approximations. The governing equations are:

$$\text{Equations of Motion:} \quad \frac{du}{dt} = \frac{-1}{\rho_0} \frac{\partial p'}{\partial x} + fv - A_m \nabla^4 u + K_m \frac{\partial^2 u}{\partial z^2} + \delta_d(u) \quad [1]$$

$$\frac{dv}{dt} = \frac{-1}{\rho_0} \frac{\partial p'}{\partial y} - fu - A_m \nabla^4 v + K_m \frac{\partial^2 v}{\partial z^2} + \delta_d(v) \quad [2]$$

$$w = - \int_{-H}^z \left(\frac{\partial u}{\partial x} + \frac{\partial v}{\partial y} \right) d\epsilon \quad [3]$$

$$\text{Hydrostatic Equation:} \quad p' = \int_z^0 \rho g d\epsilon - \frac{1}{H} \int_{-H}^0 \left(\int_z^0 \rho g d\epsilon \right) dz \quad [4]$$

$$\text{Equation of State:} \quad \rho = \rho_0 (1 - \alpha(T - T_0)) \quad [5]$$

$$\text{First Law:} \quad \frac{dT}{dt} = -A_H \nabla^4 T + K_H \frac{\partial^2 T}{\partial z^2} + Q_S + \delta_d(T) \quad [6]$$

Important features of the above equations include:

- A right-handed cartesian coordinate system is used in the above equations, with x pointing in the easterly direction, y pointing alongshore in a northerly direction, and z pointing upward. Accordingly, u is velocity in the x direction, and is positive when pointing toward the east; v is positive to the north, and w is positive upward.
- T is temperature.
- ρ is density.
- f is the Coriolis parameter.
- p' is the departure from the vertically averaged pressure (which is assumed to be zero). Because the mean pressure is assumed to be zero, the barotropic mode is considered to be ignored.
- ϵ is simply a constant of integration used in Equations (3) and (4).

- Equation (5) assumes ρ to be a function of temperature only. Any dependence on salinity is ignored.
- The terms $\delta_A(u)$, $\delta_A(v)$ and $\delta_A(T)$ represent the vertical turbulent mixing of zonal and meridional momentum and heat, respectively, due to surface layer processes, by a dynamic adjustment mechanism. This adjustment maintains the dynamic stability in the water column, in the sense of lighter water overlying denser water (Haney *et al.*, 1978).

The boundary conditions at the top ($z = 0$) of the model ocean are :

$$K_m \frac{\partial u}{\partial z} = 0 \quad [7]$$

$$K_m \frac{\partial v}{\partial z} = \frac{\tau}{\rho_0} \quad [8]$$

$$K_H \frac{\partial T}{\partial z} = -Q_B \quad [9]$$

$$w = 0 \quad [10]$$

In Equation (8), τ is the surface wind stress. In Equation (9), Q_B is the net upward flux of longwave radiation.

The bottom ($z = -H$) boundary conditions are as follow:

$$K_m \frac{\partial u}{\partial z} = C_D(u^2 + v^2)^{1/2}(u \cos \gamma - v \sin \gamma) \quad [11]$$

$$K_m \frac{\partial v}{\partial z} = C_D(u^2 + v^2)^{1/2}(v \cos \gamma + u \sin \gamma) \quad [12]$$

$$K_H \frac{\partial T}{\partial z} = 0 \quad [13]$$

$$w = 0 \quad [14]$$

In the above equations, C_D is a bottom drag coefficient and $\gamma = 10^\circ$ is the geostrophic inflow angle (Weatherly, 1972). Table 1 provides a list of other symbols found in the model equations, as well as values of constants used throughout this study.

B. MODEL DOMAIN AND RESOLUTION

The domain of both experiments in this study consists of a rectangular area, with a meridional length of 1280 km, and a zonal width of 576 km. The eastern side of the box

Table 1. VALUES OF CONSTANTS USED IN THE MODEL

	Value	Name
Ω	$2 \pi \text{ day}^{-1}$	Earth rotation rate
C	$0.958 \text{ cal gm}^{-1} \text{ }^{\circ}\text{K}^{-1}$	Specific heat of sea water
C_b	1.22×10^{-3}	Bottom drag coefficient
C_a	1.3×10^{-3}	Atmospheric drag coefficient
L	595 cal gm^{-1}	Latent heat of sea water
T_0	278.2°K	Constant reference temperature
ρ_a	$1.23 \times 10^{-3} \text{ gm cm}^{-3}$	Density of air
ρ_0	$1.0276 \text{ gm cm}^{-3}$	Density of sea water at T_0
α	$2.01 \times 10^{-4} \text{ }^{\circ}\text{K}^{-1}$	Thermal expansion coefficient
K	10	Number of levels in vertical
ΔX	$9.0 \times 10^5 \text{ cm}$	Zonal grid spacing
ΔY	$2.0 \times 10^6 \text{ cm}$	Meridional grid spacing
D or H	$4.5 \times 10^5 \text{ cm}$	Total ocean depth
ϕ_0	22.0° S	Latitude of northern boundary
ϕ_m	34.0° S	Latitude of southern boundary
λ_0	$\sim 72^{\circ} \text{ W}$	Longitude of eastern boundary
λ_m	$\sim 78^{\circ} \text{ W}$	Longitude of western boundary
Δt	800 s	Time step
g	980 cm s^{-2}	Acceleration of gravity
A_M	$2.0 \times 10^{17} \text{ cm}^4 \text{ s}^{-1}$	Bi-harmonic momentum diffusion coeff.
A_H	$2.0 \times 10^{17} \text{ cm}^4 \text{ s}^{-1}$	Bi-harmonic heat diffusion coefficient
K_M	$0.5 \text{ cm}^2 \text{ s}^{-1}$	Vertical eddy viscosity
K_H	$0.5 \text{ cm}^2 \text{ s}^{-1}$	Vertical eddy conductivity

is assumed to touch the South American coast (Figure 2). In addition, for modeling purposes, the coastline is assumed to run exactly north-south; consequently, the domain is similarly oriented. The actual coastline is relatively straight, but runs in a slight southwest to northeast direction. At 34° S the western edge of the coast is approximately 72° W ; at 22° S , the coast is located at about 70° W .

C. FINITE DIFFERENCE SCHEME

The numerical model used in this study is a staggered grid model, using the Arakawa and Lamb (1977) B-scheme. Batteen and Han (1981) have shown that this scheme is appropriate when grid spacing is approximately on the same order as, or less than, the Rossby radius of deformation, which meets the criteria of this study.

In the vertical, the model has ten layers, with constant z-levels of 13, 46, 98, 182, 316, 529, 870, 1416, 2283, and 3656 m. Consistent with Haney (1974), this spacing scheme concentrates more on the upper, dynamically active part of the ocean, above the thermocline.

D. HEAT AND MOMENTUM DIFFUSION

Because this study is designed to investigate the generation of mesoscale eddies along the coast of Chile, the type of diffusion used in the model equations becomes an important issue. Laplacian lateral heat diffusion tends to suppress the formation of mesoscale eddies by diminishing baroclinic signals at that scale, thus making it more difficult for baroclinic instabilities to overcome diffusive damping (Holland and Batteen, 1986). Biharmonic diffusion, on the other hand, tends to allow the formation of mesoscale instabilities, because it tends to damp at scales smaller than mesoscale eddies (Batteen *et al.*, 1989). For these reasons, biharmonic lateral heat and momentum diffusion are used in this paper. Coefficients are listed in Table 1.

E. SURFACE THERMAL FORCING

To isolate the effects of wind forcing in these process-oriented studies, the net heat flux at the sea surface should initially be zero. In this way, any heat flux that is generated will have been generated by an increase or decrease of sea surface temperature resulting from wind forcing effects (Batteen *et al.*, 1989). To accomplish this, surface generated heat flux ($\overline{w'T'}$) is set equal to (S_0), which is defined as the solar radiation at the sea surface (Haney *et al.*, 1978). Simply stated:

$$S_0 - (\overline{w'T'}) = 0. \quad [15]$$

These terms and their components are in turn broken down into the following mathematical definitions:

$$S_0 = S_0^* / \rho_0 C \quad [16]$$

$$(\overline{w'T'})_0 = (Q_B + Q_S + Q_E) / \rho_0 C \quad [17]$$

$$S_0^* = 0.95(0.74 - 0.6n)S_A^* \quad [18]$$

$$S_A^* = 3.642 \times 10^{-3} \quad [19]$$

$$Q_B = 0.985\sigma(T_S)^4 \times [0.39 - 5.0(e_A)^{1/2}](1 - 0.6n^2) \quad [20]$$

$$Q_S = \rho_A C_H C_p |V| (T_S - T_A) \quad [21]$$

$$Q_E = \rho_A C_H L |V| (0.622/p_A)(e_S - e_A) \quad [22]$$

The variables used in these equations are defined in Table 2. Values for T_S , n , p_A , e_A , specific and relative humidity (used to compute e_S) are all taken from Esbensen and Kushnir (1981), while solar insolation values are taken from List (1984). To estimate annual means, the values were averaged over twelve months. Using these values, the ambient air temperature that results in zero heat flux at the surface is 290.13° K.

F. BOUNDARY CONDITIONS

The rectangular box surrounding the model domain is bordered on the northern, southern and western edges by open ocean. The eastern edge is assumed to border the western coast of Chile; it is a no-slip, straight vertical wall extending from the surface to 4500 *m* depth. At this eastern boundary, both tangential (*y* direction) and normal (*x*

Table 2. VARIABLES USED IN COMPUTING NET HEAT FLUX

	Value	Description
S_0	Equation 16	Solar radiation at sea surface
$\overline{w'T'}$	Equation 17	Surface generated heat flux
S_0^*	Equation 18	Downward flux of solar rad
S_A^*	Equation 19	Flux of solar radiation at top of atmosphere
Q_b	Equation 20	Net upward longwave rad
Q_s	Equation 21	Sensible heat flux
Q_e	Equation 22	Latent heat flux
τ	1 dyne/cm ²	Wind stress
C	0.958 cal g ⁻¹ °C ⁻¹	Spec heat of sea water
C_p	0.24 cal g ⁻¹ °C ⁻¹	Spec heat of dry air
n	0.63	Fractional cloud cover
	5 %	Reflectivity of sea surface
	26 %	Reduc of insol by atmos absorp
C_H	1.757×10^{-3}	Heat exchange coefficient
$ V $	830 cm/s	Wind speed
T_s	16.72° C	Sea surface temp
T_a	290.13° K	Ambient air temp
ρ_A	.00123 g cm ⁻³	Air density at sea level
σ	1.35×10^{-12}	Stefan-Boltzmann constant
e_s	20.8 mb	Saturation vapor press at T_s
e_a	16.49 mb	Atmos vapor pressure
p_A	1013.25 mb	Atmos press at sea level

direction) components of velocity go to zero. A flat bottom at 4500 *m* is assumed throughout the entire domain. Both of the above assumptions can be justified for two reasons. First, because this is a process-oriented study, the inclusion of a rough coastline or bottom would induce additional shears and curl values (compared to those induced by a flat bottom and straight vertical coastline as in Batteen *et al.* (1989) and Fonseca (1989)), with the result that the particular process being investigated (i.e., wind

forcing) would not be isolated. Second, the Chilean coastline is relatively straight and smooth, the continental shelf is relatively narrow, and the continental slope is steep, dropping from sea level to over 1000 fathoms (~ 2000 m) in a distance of less than 25 km from the coast (Ziegler *et al.*, 1957). Therefore, the use of a straight, vertical wall is not too unreasonable an approximation for a process-oriented study designed to isolate the effects of wind forcing on the Chilean Current System.

G. INITIAL CONDITIONS

Climatological vertical and horizontal temperature profiles, derived from Levitus (1982), show that, over the study domain, the average seasonal surface temperatures vary between a summertime maximum of roughly 22° C at $\sim 22^{\circ}$ S, to a wintertime minimum of 13° C at $\sim 34^{\circ}$ S. The average annual sea surface temperature for the area is 17° C. Although a relatively weak north-south temperature gradient is evident at all depths, seasonal variations are negligible below 100 m depth.

A temperature profile based on Levitus (1982) was used in both experiments to represent the initial temperature conditions for the model domain. The method for incorporating the values of the profile into the model was similar to that used in Batteen and Rutherford (1990). Initially, mean annual temperatures were taken from Levitus (1982) for applicable 5° squares in or adjacent to the model domain, then interpolated in an east-west direction to match the middle of the domain. The temperature profile at each point was then interpolated vertically to correspond to the midpoints of the ten layers used in the model. These computations resulted in two "smoothed" temperature profiles, one representing the northern part of the domain (centered at 17.5° S), and the other representing the southern region (centered at 37.5° S). These two profiles were interpolated once again, this time in a north-south direction, to obtain an annual temperature profile, centered at 28° S.

As in Batteen *et al.* (1989, 1991) an exponential curve was then used to approximate the climatological temperature profile that had been computed from Levitus (1982). The form of the equation used was:

$$T(z) = T_S + \Delta T e^{z/h}. \quad [23]$$

The approximation uses a length scale of 450 *m*, and assumes $T_S = 2^\circ \text{C}$ to be the temperature at great depth. $\Delta T = 15^\circ \text{C}$ is the change of temperature between the bottom and top of the profile. Figure 3 shows that the resulting temperature profile fits the mean annual interpolated profile. This exponential profile was used to provide initial values at each of the ten levels in the model.

H. EXPERIMENTAL CONDITIONS

1. Experiment One: Constant Wind Stress

In the first experiment, a constant equatorward wind stress of 1 *dyne/cm*² ($\sim 830 \text{ cm/s}$) is applied to all gridpoints within the domain, except for a band at the northern and southern ends, where no wind forcing is applied. McCreary (1981) demonstrated that this technique allowed for the propagation of coastal Kelvin waves, which in turn allowed for the creation of an undercurrent and a coastal jet (Batteen *et al.*, 1989). Because the winds are predominantly equatorward all year off Chile, the model is run for 240 days, which is a sufficient time for currents and eddies to develop in the model.

2. Experiment Two: Variable Climatological Winds

In Experiment 2, daily climatological winds are used to simulate the temporal and spatial wind variations that have been observed off the coast of Chile. Data, in the form of climatological wind stress fields, are taken from Bakun and Nelson (1991). The wind stress fields were derived from all available ship wind reports that have been collected in the region between 1850-1979, after eliminating physically unrealistic reports.

Figures 4 and 5, taken from Bakun and Nelson (1991), show the wind stress and wind stress curl fields, respectively, that are used. The wind stress fields are grouped into one-degree square regions (their midpoints being on the intersections between integer latitudes and longitudes), and a monthly mean value is computed for each region.

Because wind speed values (vice wind stress values) are used in the model, wind speed values were obtained using the following equation:

$$U = \sqrt{\frac{\tau}{\rho_A C_d}}, \quad [24]$$

where τ is wind stress, ρ_A is air density, C_d is the atmospheric drag coefficient, and U is wind speed. The resulting wind values were then smoothed using a nonlinear 3 X 3 median smoothing technique described in Rabiner *et al.* (1975), and used successfully in Batteen *et al.* (1991). This technique was shown in Rabiner *et al.* (1975) to preserve the significant features in a field that can otherwise be hidden or "smoothed-out" when a linear filter is used. After smoothing, the resulting wind values for the 12° latitude by 6° longitude region being studied were interpolated onto a 65 X 65 grid, basically covering the same geographical area. The easternmost gridpoints were considered to be touching the continent. The resulting twelve monthly wind fields were then linearly interpolated into 365 daily fields, which were used to simulate one year's worth of daily, climatological wind values. In their final form, the data consisted of 365 grids (65 X 65), each gridpoint having a unique interpolated value. In the model, the appropriate day's values are read at the beginning of each integer day. An example of the wind fields can be seen in Figure 6, which shows the annual migration of maximum winds from the south in the austral summer, to the north in the austral winter months, the effects of which are discussed in Chapter V.

It should be kept in mind that the daily wind values are a linear interpolation of monthly climatological winds, and not daily climatological values. As a result, the

values should be considered as linear extensions of month-to-month trends, divided into daily values to allow for a smooth transition from one monthly mean to the next.

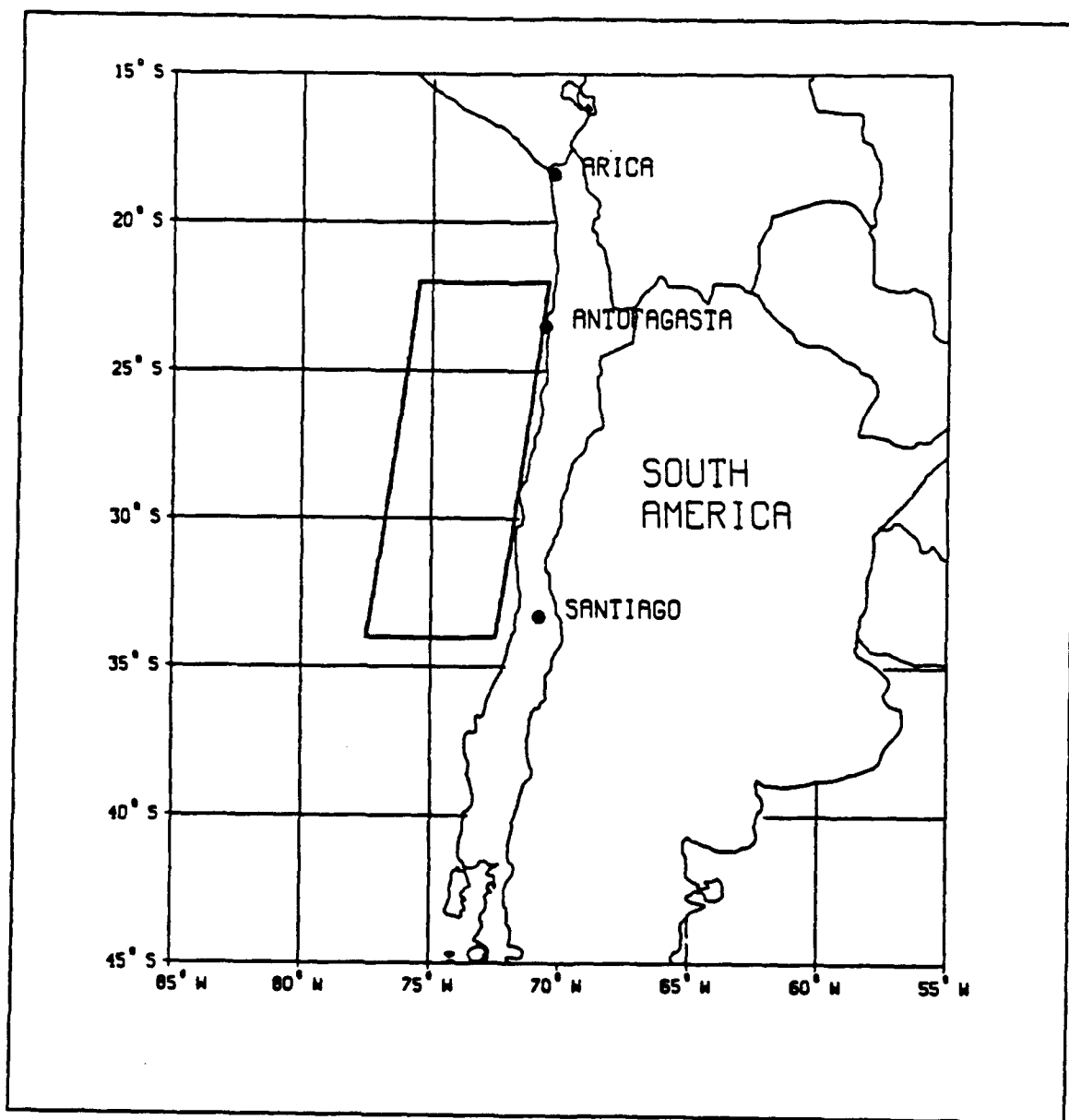


Figure 2. Model Domain: Area of study is a 576 km by 1280 km box off the coast of Chile.

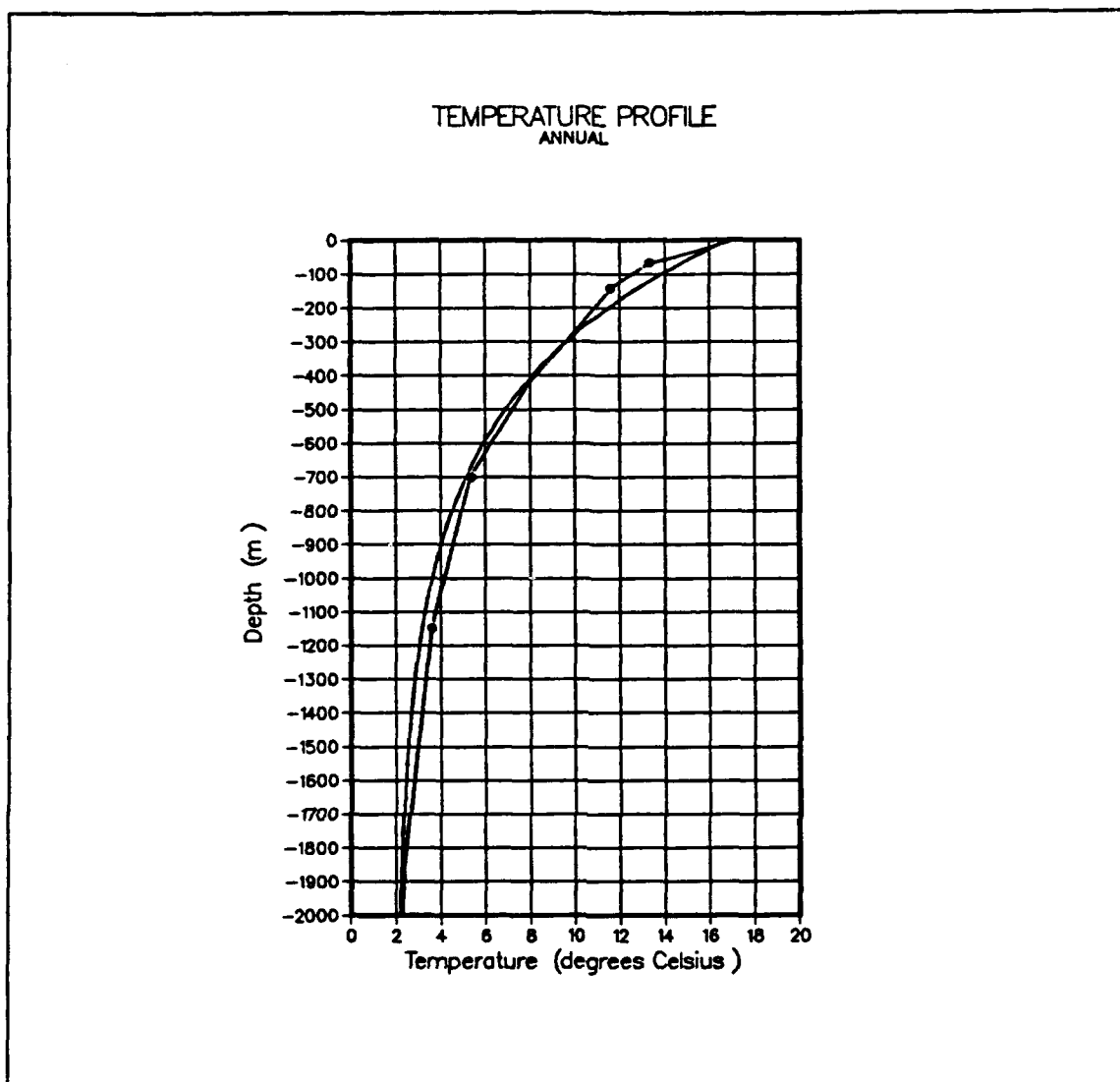


Figure 3. Temperature profile used in both experiments: A smooth exponential curve (solid line) was used to approximate the climatological temperature profile (solid line with small circles) computed from Levitus (1982).

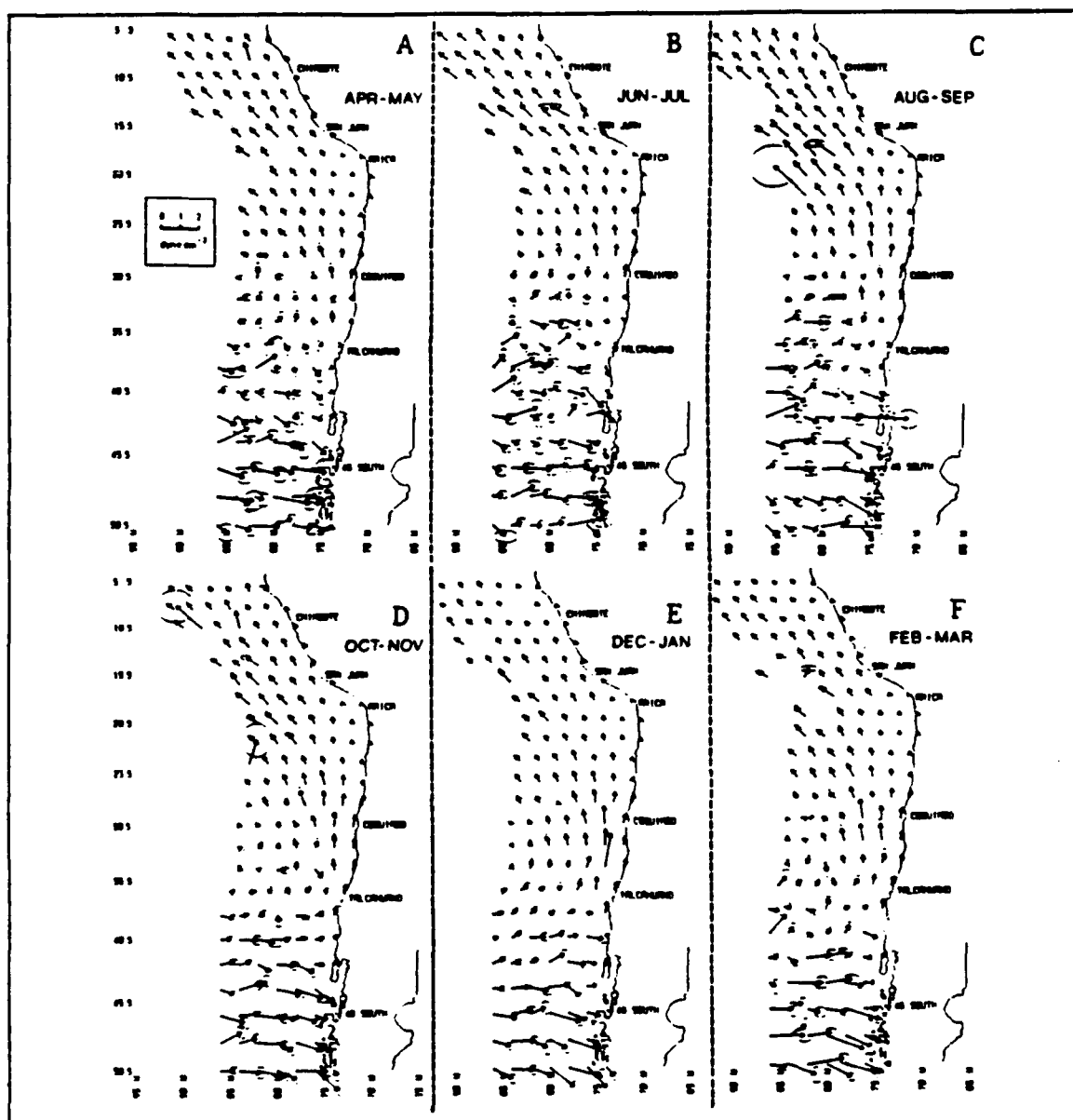


Figure 4. Wind stress fields from Bakun and Nelson (1991): Vectors are scaled in units of dyne/cm^2 . Ellipses show areas of large standard errors (discussed in Bakun and Nelson, 1991).

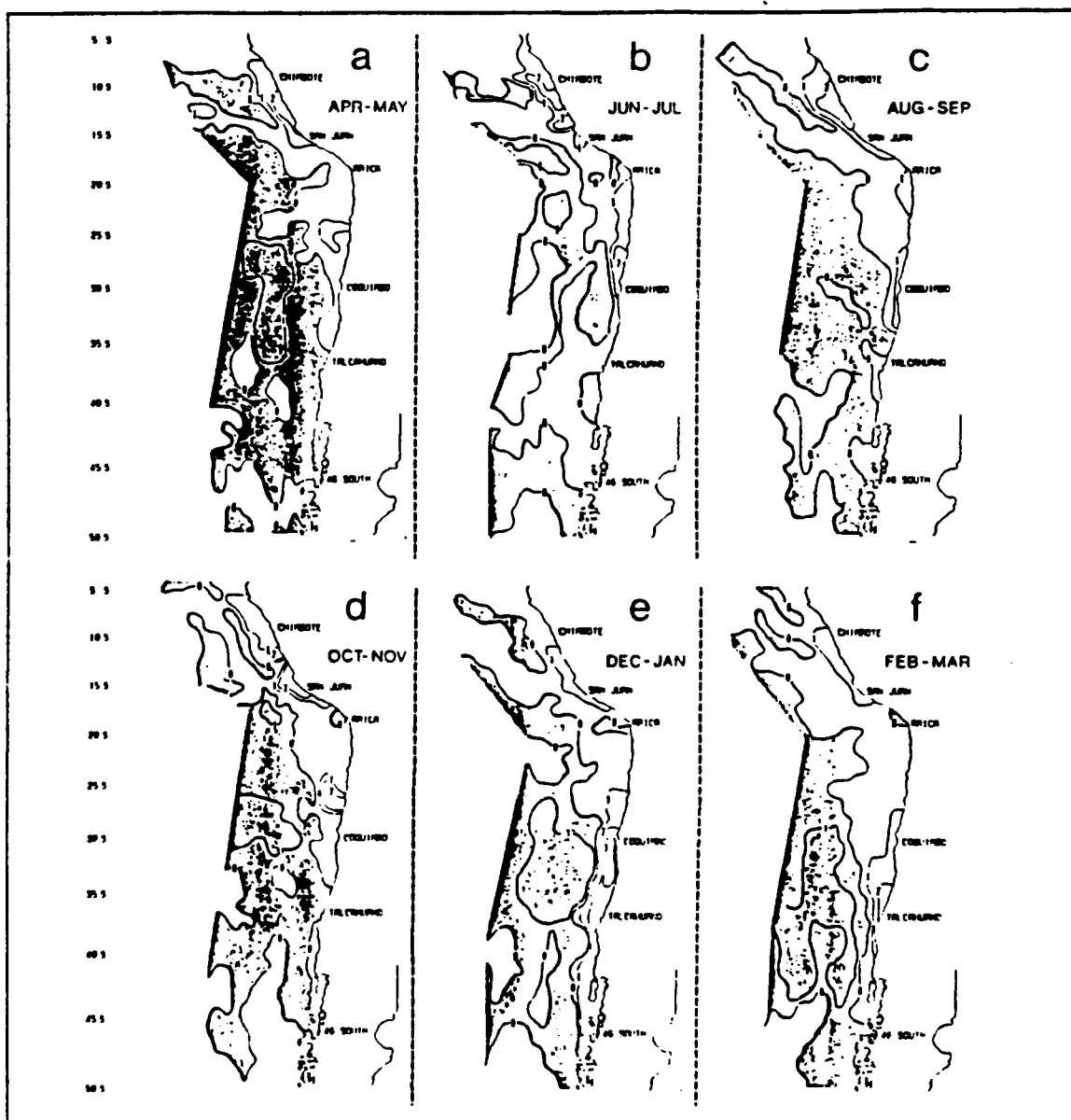


Figure 5. Wind stress curl fields from Bakun and Nelson (1991): Units and contour interval are $10^{-8} \text{ dyne/cm}^2$. Regions of anticyclonic curl are shaded.

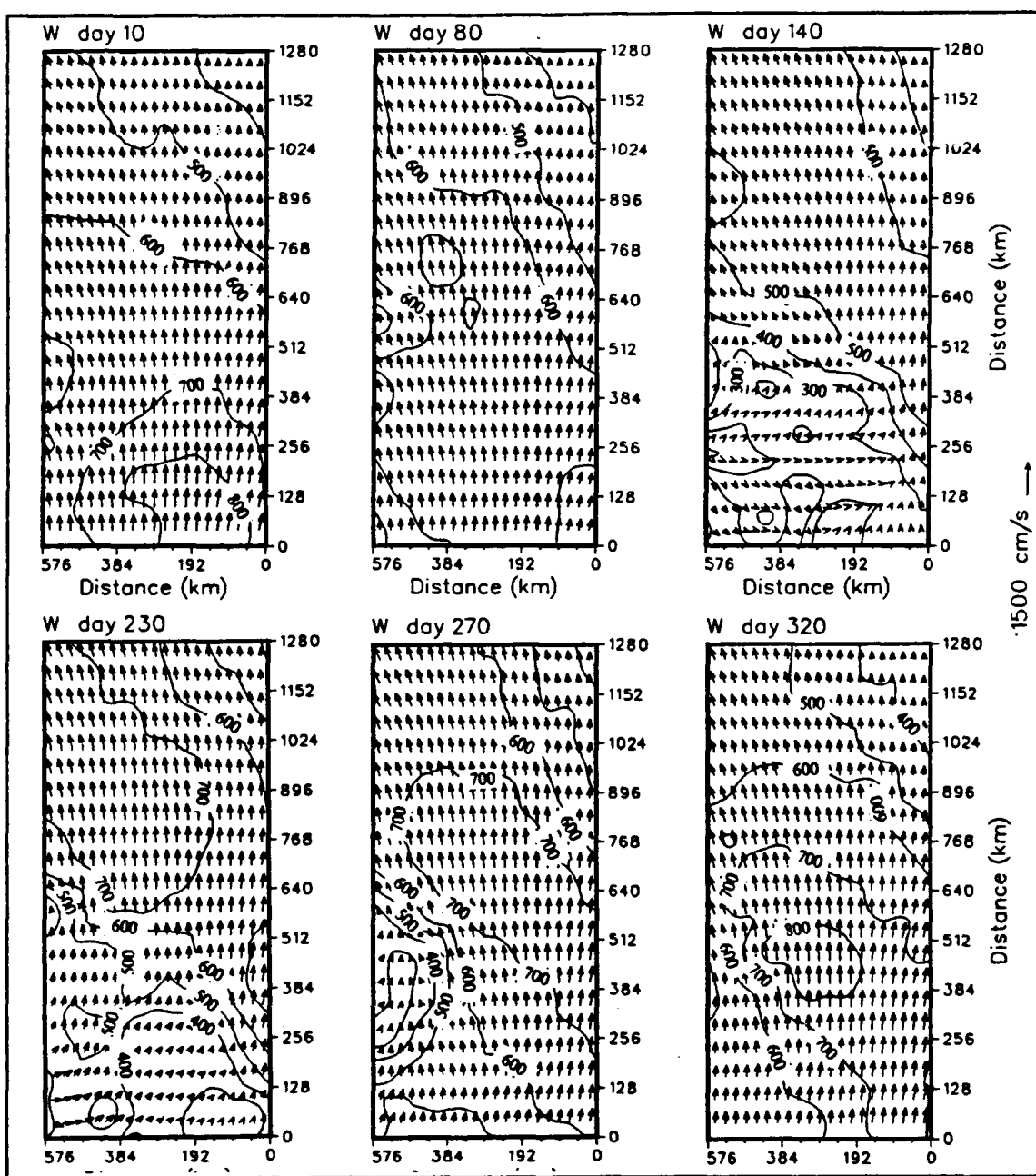


Figure 6. Wind speed vectors with magnitude contours: Vectors are scaled in units of cm/s . Contours are in hundreds of cm/s . Day 1 corresponds to 1 January.

IV. ANALYSIS TECHNIQUES

The following energy and spectral techniques, adapted from Batteen and Rutherford (1990), will be used in the following chapter to analyze the generation and stability of the Peru-Chile Current and eddies.

A. ENERGY ANALYSIS

An energy analysis based on that of Han (1975) and Semtner and Mintz (1977) is made to gain a better understanding of the energy transfers in the unstable flow. The energy calculations are presented using the Semtner and Mintz (1977) notation:

$\overline{(\quad)}$	time average
$(\quad)'$	time deviation
$\tilde{(\quad)}$	horizontal space average
$(\quad)'$	horizontal space deviation.

The kinetic energy (K) is calculated by:

$$K = \frac{u^2 + v^2}{2} \quad [25]$$

and presented in a time series plot. After reaching a quasi-steady state in which the total kinetic energy is nearly constant, the time mean and time eddy kinetic energy are calculated by:

$$\bar{K} = \frac{\bar{u}^2 + \bar{v}^2}{2} \quad [26]$$

$$K' = \frac{\overline{u'^2} + \overline{v'^2}}{2} \quad [27]$$

Available potential energy (P) is calculated by:

$$P = \alpha g \left[\frac{1}{2} (T^*)^2 \left(\frac{\partial \tilde{T}}{\partial z} \right)^{-1} \right]. \quad [28]$$

The temporal mean and eddy available potential energy are calculated by:

$$\bar{P} = \alpha g \left[\frac{1}{2} (\bar{T}^*)^2 \left(\frac{\partial \tilde{T}}{\partial z} \right)^{-1} \right] \quad [29]$$

$$P' = \alpha g \left[\frac{1}{2} (\overline{T^*})^2 \left(\frac{\partial \tilde{T}}{\partial z} \right)^{-1} \right]. \quad [30]$$

The transfers between the energy types are defined, after Semtner and Mintz (1977), by:

$$\{\bar{K} \rightarrow \bar{P}\} = -\alpha g [\bar{T} \bar{w}] \quad [31]$$

$$\{P' \rightarrow K'\} = \alpha g [\overline{T w'}] \quad [32]$$

$$\{\bar{K} \rightarrow K'\} = \bar{v} \cdot \left(\nabla \cdot \overline{v' v'} + \frac{\partial}{\partial z} \overline{w' v'} \right) \quad [33]$$

$$\{\bar{P} \rightarrow P'\} = \alpha g \left[\bar{T} \nabla \cdot \overline{v' T^*} \left(\frac{\partial \tilde{T}}{\partial z} \right)^{-1} \right]. \quad [34]$$

The model output consists of velocity components and temperature at daily intervals at each gridpoint and neither the vertical velocity nor any advection terms calculated by the model are stored. Because the calculation of the energy transfers requires both vertical velocity and numerous advection terms, these were recalculated in the same manner as in the model but using the stored values of u , v and T as the input data. Although

the energy transfers are recalculated from model output, they are consistent with the initial calculations of vertical velocity and advection terms in the model.

Semtner and Mintz (1977) applied their energy transfer analysis to currents which had become unstable, generated eddies and then reached a quasi-steady state. In this study, the quasi-steady energetic state prior to eddy generation is examined, and the energy transfers are used to argue for the instability mechanism which leads to the initial eddy generation in each case.

B. SPECTRAL ANALYSIS

A spectral analysis technique is used to estimate the dominant wavelengths at which eddy growth occurs. The alongshore wavenumber is selected based on an assumption of a meridional anisotropic preference for the eddy development. The model configuration of 65 alongshore temperature gridpoints and 64 velocity points is ideal in allowing data over the entire domain to be used to compute the discrete Fourier transform based on 64 points. Leakage due to the finite length of the series is reduced using a Hanning window. The loss of variance due to the windowing is then compensated by scaling the calculated one-sided spectral density appropriately.

V. RESULTS OF THE WIND FORCING EXPERIMENTS

Experiment 1 studies the effects of steady, upwelling-favorable winds in the Chile eastern boundary current region. Experiment 2 investigates the effects of seasonally varying winds in the same region, using climatological monthly values that have been interpolated to daily values.

A. EXPERIMENT 1

In Experiment 1, a constant wind stress was applied to the interior of the domain for 240 days. As in Batteen *et al.* (1991), inertial oscillations of near-surface ocean currents developed initially. After a few days of model simulation time, the oscillations were damped, leaving quasi-steady offshore Ekman transport, as shown by the surface velocity vectors in Figure 7A. Figures 7B, 7C and 7D indicate that an equatorward-flowing, upwelling-favorable surface current had been generated. A poleward-flowing undercurrent (not shown) had also developed. The surface current flowed at ~ 20 cm/s, and extended ~ 50 km offshore, while the undercurrent, centered along the coast at ~ 300 m depth, had weaker velocities of ~ 4 cm/s.

The first evidence of developing eddies occurred by day 50, as evidenced by the appearance of perturbations in the zonal velocity fields (Figure 8). (Perturbations are more clearly seen in these types of presentations than in meridional velocity plots, because the latter tend to be dominated by the currents, which are predominantly in the meridional direction.) The time sequence of surface zonal velocity shows the development and growth of eddies from days 50-160. The baroclinic and barotropic transfers (based on Equations (32) and (33), respectively), are given in Figure 9, and show that both types of instabilities contribute to the development of eddies in the region. Barotropic instability is evident near the offshore region of the coastal jet and near the

coastline because of the horizontal shear in the region. Baroclinic instability, which draws its energy from the vertical shear in the mean flow (Haltiner and Williams, 1980; Batteen *et al.*, 1991), was evident in the interior of the coastal region.

By day 60, meanders were evident at $y \sim 250$ to 500 km near the coast in the velocity, dynamic height and temperature fields, as seen in Figures 10A-10D. As in the β -plane experiment of Batteen *et al.* (1989), eddies first formed in the poleward end of the region, as expected. Figures 10 and 11 show that the dominant wavelength at day 60 is ~ 100 km.

Figure 12 shows three meridional velocity cross-sections averaged over days 50 - 60. The three cross-sections correspond to areas near the equatorward, middle, and poleward parts of the model domain, respectively. Figure 12 shows that the surface current has a width of ~ 100 km, and an average velocity of ~ 18 cm/s, while the undercurrent has a core velocity of ~ 10 cm/s at ~ 250 m depth. The undercurrent weakens towards the equator and intensifies near its poleward end.

Figure 13 shows the fields of surface velocity vectors, temperature, velocity contours, and dynamic heights (relative to 2000 m) at day 120. The perturbations and meanders seen earlier in the southern part of the domain (see Figure 7) have developed into anticyclonic and cyclonic eddies. For example, a cyclonic eddy is discernible at $y \sim 256$ km with a corresponding cold core temperature of $\sim 14.5^\circ$ C. Figure 14 shows that, although both barotropic and baroclinic instability processes contribute to the formation and development of eddies, barotropic energy transfer is dominant, due to the larger energy transfer. Figure 15 indicates that the surface current has intensified to > 20 cm/s near the poleward end of the domain. The undercurrent maintains a core velocity of $\sim 5 - 10$ cm/s, and is better developed at ~ 620 km than towards the pole.

Closed eddies were fully formed by day 160 (Figures 16A and 16D). While average values of the coastal surface current were ~ 30 cm/s (not shown), a maximum value of

~ 40 cm/s was reached by day 160 (Figure 16C). A cold, offshore-flowing filament extends to ~ 350 km offshore (Figure 16B). Figure 17 shows that the current extends to $\sim 150 - 200$ m depth in the equatorward end of the domain, while the undercurrent core is at ~ 350 m and centered at ~ 10 km offshore (except at the poleward end, where the core is at the coast). Figure 18 shows that the dominant wavelength was ~ 250 km.

The maximum velocity of the undercurrent was reached by day 210, when it reached a magnitude of ~ 25 cm/s (Figure 19). The core moves from ~ 10 km (Figure 19A) to ~ 40 km (Figure 19C) offshore from north to south. What appeared to be a surface countercurrent in Figure 19 is most likely a manifestation of a cyclonic eddy that had formed in that area, with its poleward-flowing eastern side dominating the equatorward-flowing mean surface flow. This is supported by Figure 20D, which shows an upwelling-favorable low height center in the same region ($y \sim 300$ km), accompanied by a corresponding cold core center. Figures 20A and 20C both show poleward components in the vicinity of the eastern edge of the cyclonic eddy. Also evident are cold, offshore-flowing filaments extending as far as ~ 400 km offshore, as seen in Figure 20B.

B. EXPERIMENT 2

In Experiment 2, daily-varying wind forcing, corresponding to interpolated monthly climatological values taken from Bakun and Nelson (1991), were used in the model. The experiment ran from day 1 (corresponding to January 1) to day 365. In the early part of the experiment, which corresponded to the middle of the austral summer, winds were generally meridional throughout the domain (see Figure 6), and the South Pacific anticyclonic gyre was at its southernmost extent. Figure 5, taken from Bakun and Nelson (1991), also shows a relative wind stress curl minima in the northeast corner of the domain during the summer months. This would imply that upwelling would be enhanced in the southern portion of the domain, where cyclonic wind stress curl values were higher. As was the case in Experiment 1, an equatorward surface current was es-

established by day 20, extending ~ 80 km off the coast and reaching a magnitude of > 20 cm/s. An undercurrent first appeared at day 20 in the southern extreme of the region, but by day 40 was present all along the coast, with a core ~ 10 km offshore, at ~ 350 m depth (see Figure 21).

A series of temperature cross-sections at day 50 (Figure 22) shows upward bending of isotherms near the coast, which is consistent with a more intense upwelling regime in the southern than in the northern part of the region. A planar view of the surface temperature at day 50 (Figure 23B) also shows a wider swath of cooler, upwelled water in the south, and a narrower band in the north. Surface velocity vector, zonal velocity, and dynamic heights in Figures 23A, 23C and 23D, respectively, show that, in contrast to Experiment 1, eddies had not yet formed by day 50, and velocities tended to be smaller, perhaps because of the weaker winds (generally less than 800 cm/s) throughout most of the region.

The first evidence of perturbations was seen by day 80 (Figure 24). Meanders occur ~ 100 km to 200 km further to the north than their counterparts in Experiment 1. The reason for the difference between the two experiments was due to the different wind forcings used (i.e., uniform versus seasonally varying winds), because all other conditions remained the same. Spectral density analysis reveals a smaller wavenumber than had been present in Experiment 1, corresponding to a wavelength of ~ 85 km (Figure 25), (also seen in Figure 24, when eddies are being generated). Figure 26 shows that by day 80 a weak, poleward flowing undercurrent is only evident in the middle and southern portions of the region, centered within 20 km of the coast, at a depth of ~ 300 m. Also shown is a surface current extending ~ 80 km off the coast, to a depth of ~ 150 m.

By day 140, the South Pacific High had migrated to the north, allowing a westerly, diffluent wind pattern to develop in the southern part of the domain (Figure 6), while winds in the north remained meridionally oriented. A time sequence of dynamic height

fields (Figure 27) shows that eddies were well developed by day 140, with larger eddies forming in the north, and smaller eddies in the south. As discussed in Batteen and Rutherford (1990), in a β -plane regime, barotropic instability tends to support eddies with radii greater than the Rossby radius of deformation, whereas baroclinic instability tends to support growth on the same order as the Rossby radius of deformation. As Figure 28 indicates, barotropic instability is prevalent through most of the coastal regions, while baroclinic instability tended to dominate only in the extreme south, below the region of diffluent winds. Because this effect was not seen in Experiment 1, the varying winds must have been the cause of the different sized eddies. By day 140 the swath of cooler, upwelled temperatures was no longer wider in the south (Figure 29). Instead, the widest band of cool temperatures was found in the north, once again likely due to the diffluent winds in the south, which tended to blow towards the coast rather than along it (Figure 6). In Figure 29, the time sequence of sea surface temperature contours also shows the development of cold filaments from days 80 to 140.

By day 250, the winds had transitioned back into primarily a meridional regime (Figure 6). The time-averaged surface current had increased to $> 50 \text{ cm/s}$ along the middle of the coast by day 250 (Figure 30), where wind magnitudes were greatest (Figure 6). The dominant wavelength (Figure 31) had increased to $\sim 250 \text{ km}$, which corresponded to the large eddies in the north. Smaller eddies were still evident in the south, and, as indicated in Figure 31, had become nearly as energetically significant as the eddies at longer wavelengths. The smaller scale eddy generation occurred during a period of primarily meridional, equatorward winds.

Figure 32 shows a time sequence of surface dynamic height fields from days 250 to 280, when a cyclonic, cold-core eddy at $y \sim 700 \text{ km}$ breaks off and transits to the west. Figure 33 shows a time sequence of dynamic height fields towards the end of the year, when an anticyclonic, warm core eddy at $y \sim 768 \text{ km}$ travels eastward, into the region

of lower dynamic heights, possibly in response to a more meridionally oriented wind field.

The equatorward surface current, which reached a maximum speed of ~ 50 cm/s by late austral spring (when winds had returned to a meridional orientation throughout the region), remained relatively constant throughout the duration of the experiment. The average magnitude of the undercurrent (averaged over 30 days to filter out eddies) was ~ 15 cm/s, at the end of the model simulation, when the South Pacific High had shifted back to the southern part of the domain. The largest instantaneous velocity of the undercurrent (not shown) was ~ 32 cm/s, occurring in the southern part of the region at day 360.

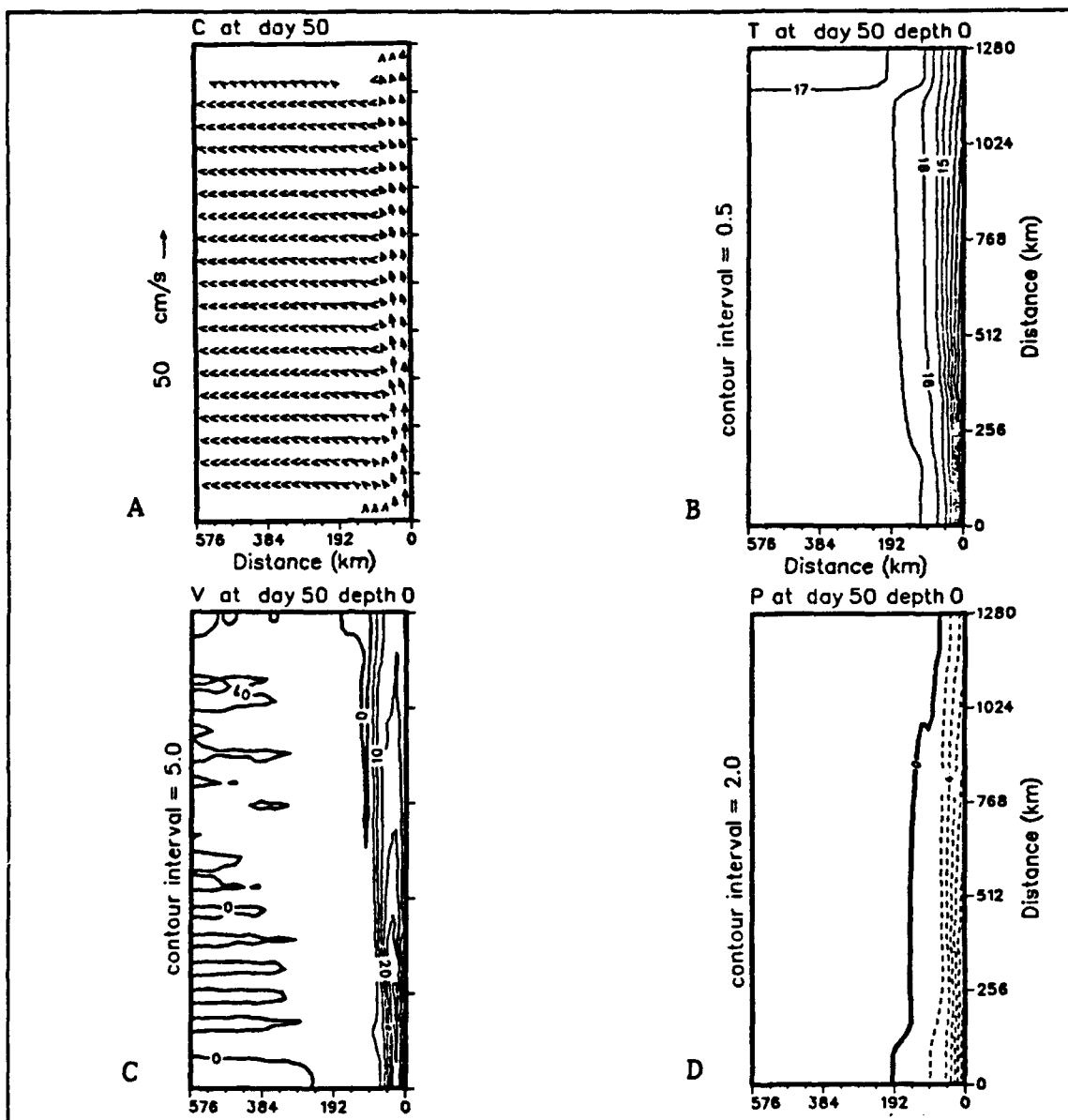


Figure 7. Surface current vectors, temperature, meridional velocity and dynamic height at day 50 of Experiment 1: Velocities are in cm/s , T is in $^{\circ}C$, heights are in cm relative to 2000 m . Dashed lines are negative height values.

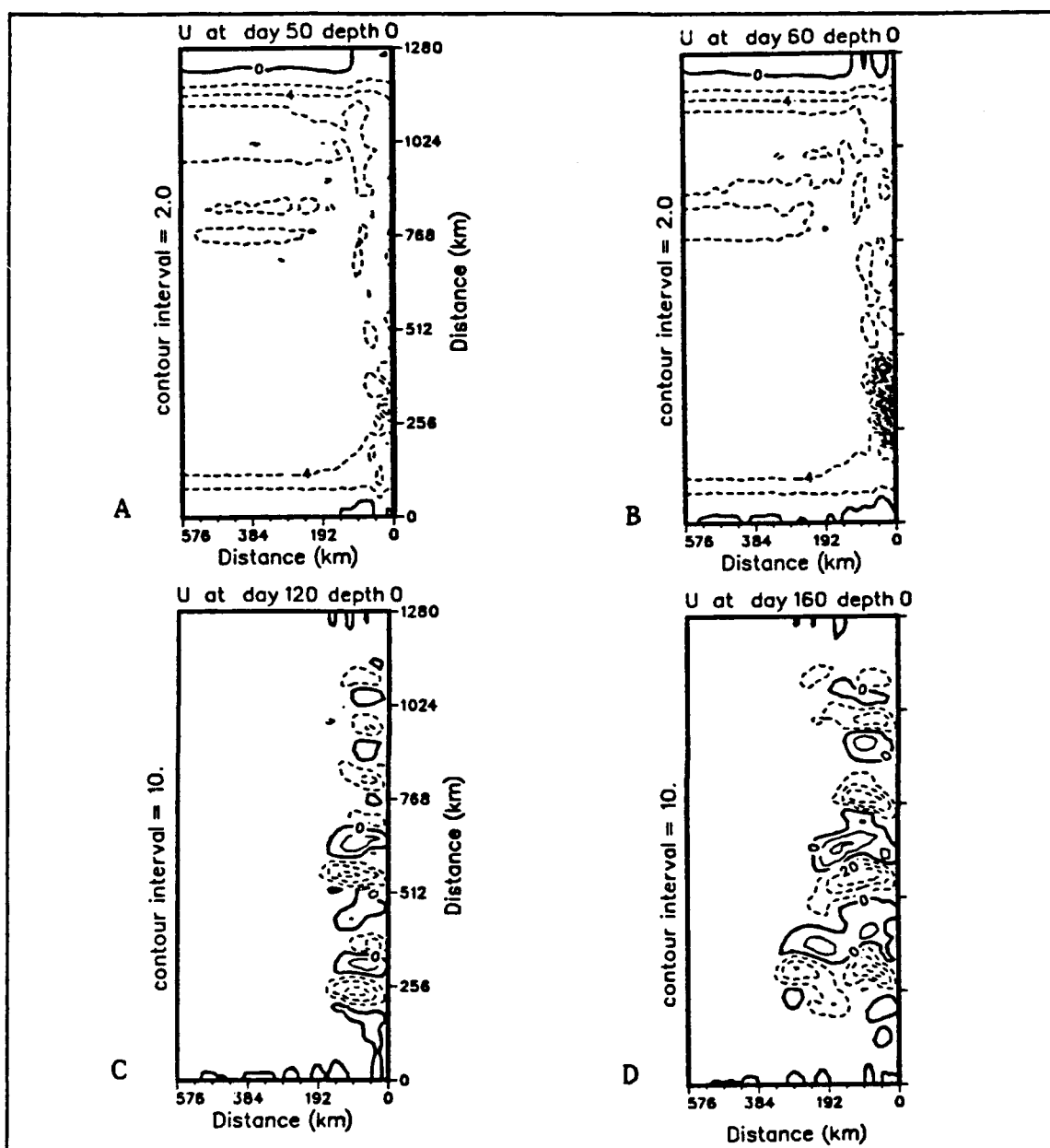


Figure 8. U (surface zonal velocity) for Experiment 1: Velocities are in *cm/s*.

Dashed lines denote westward velocities.

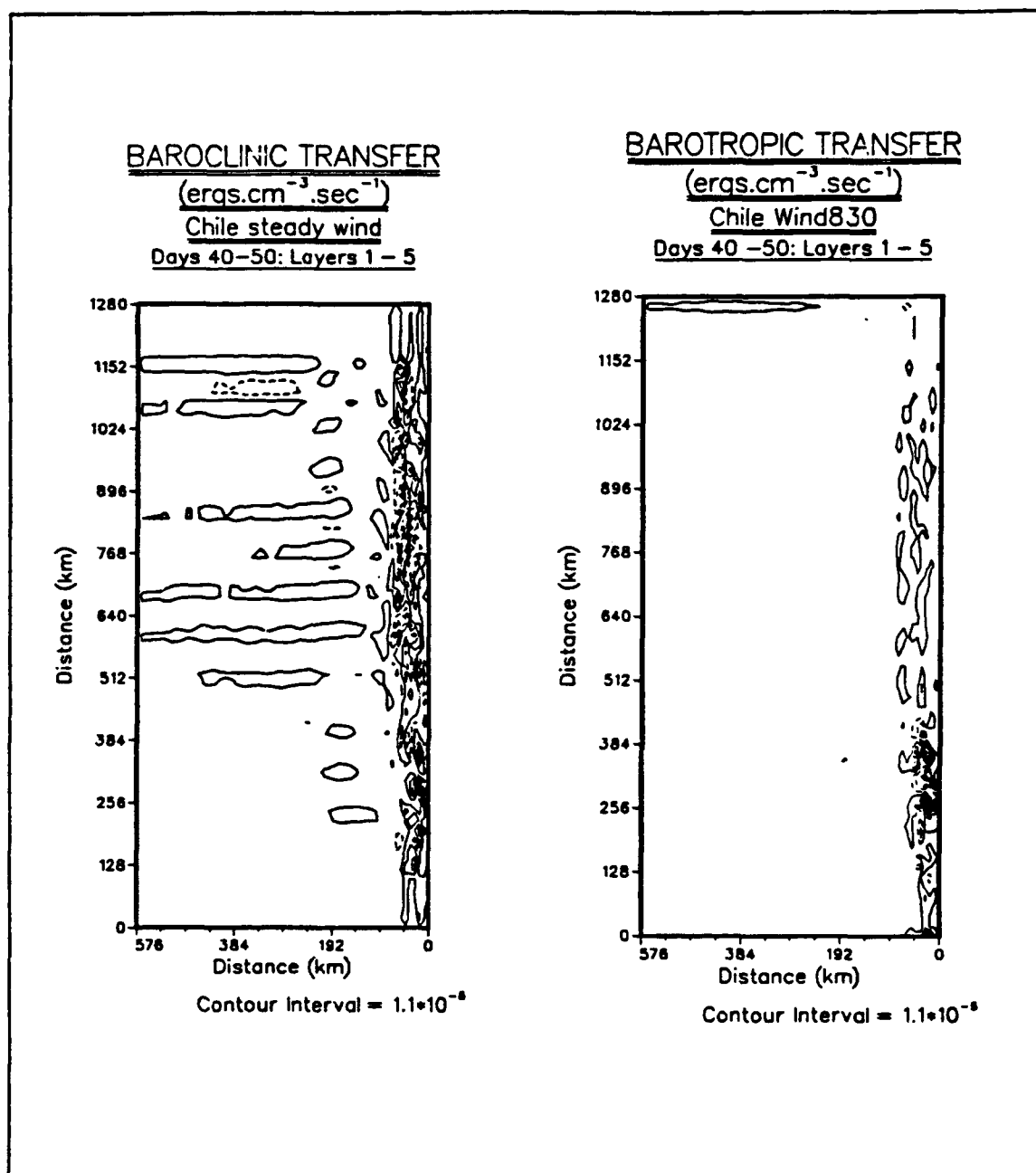


Figure 9. Baroclinic and barotropic instability at day 50 of Experiment 1.

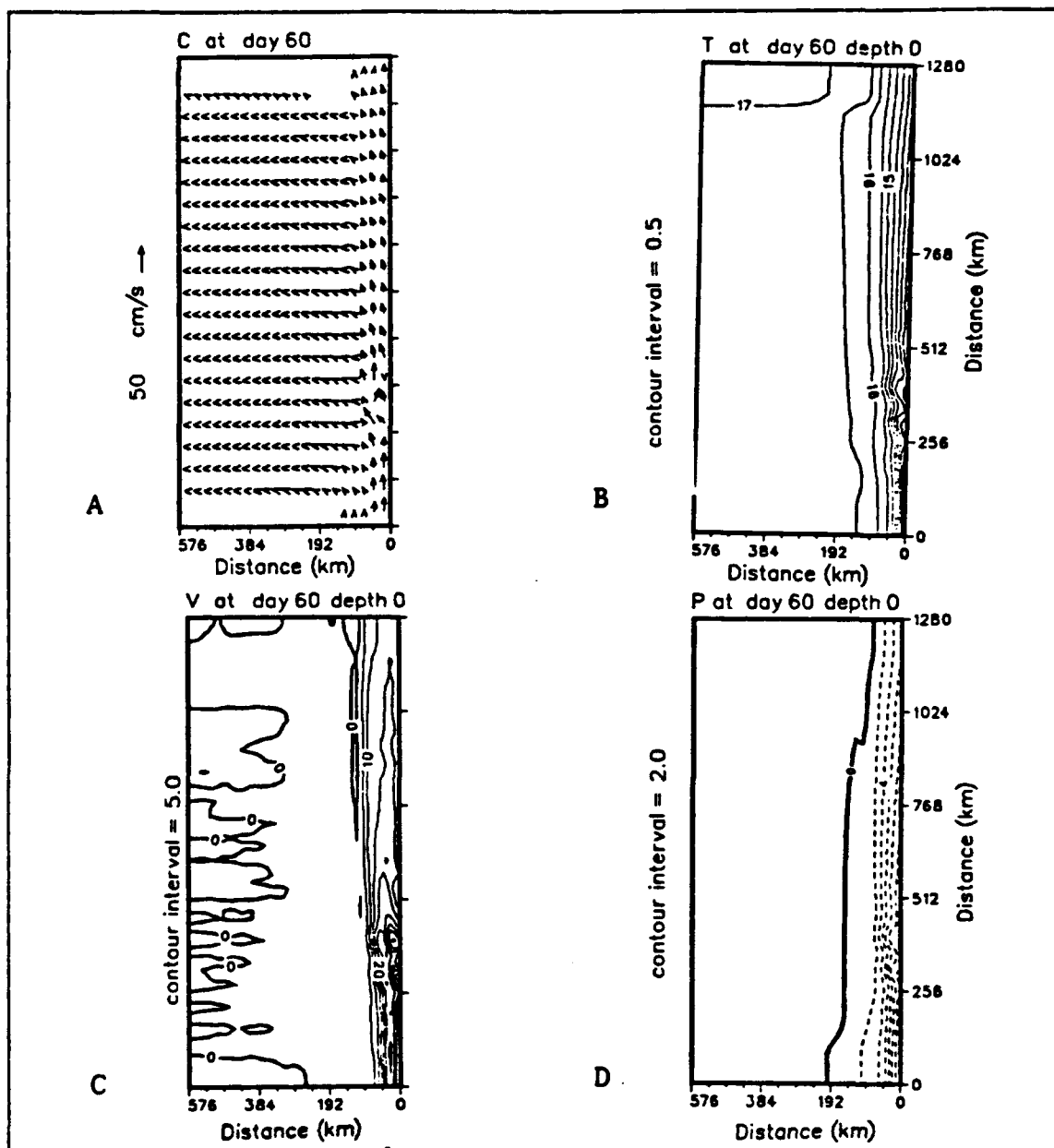


Figure 10. Surface current vectors, temperature, meridional velocity and dynamic height at day 60 of Experiment I: Velocities are in cm/s , T is in $^{\circ}C$, heights are in cm relative to 2000 m . Dashed lines denote negative values.

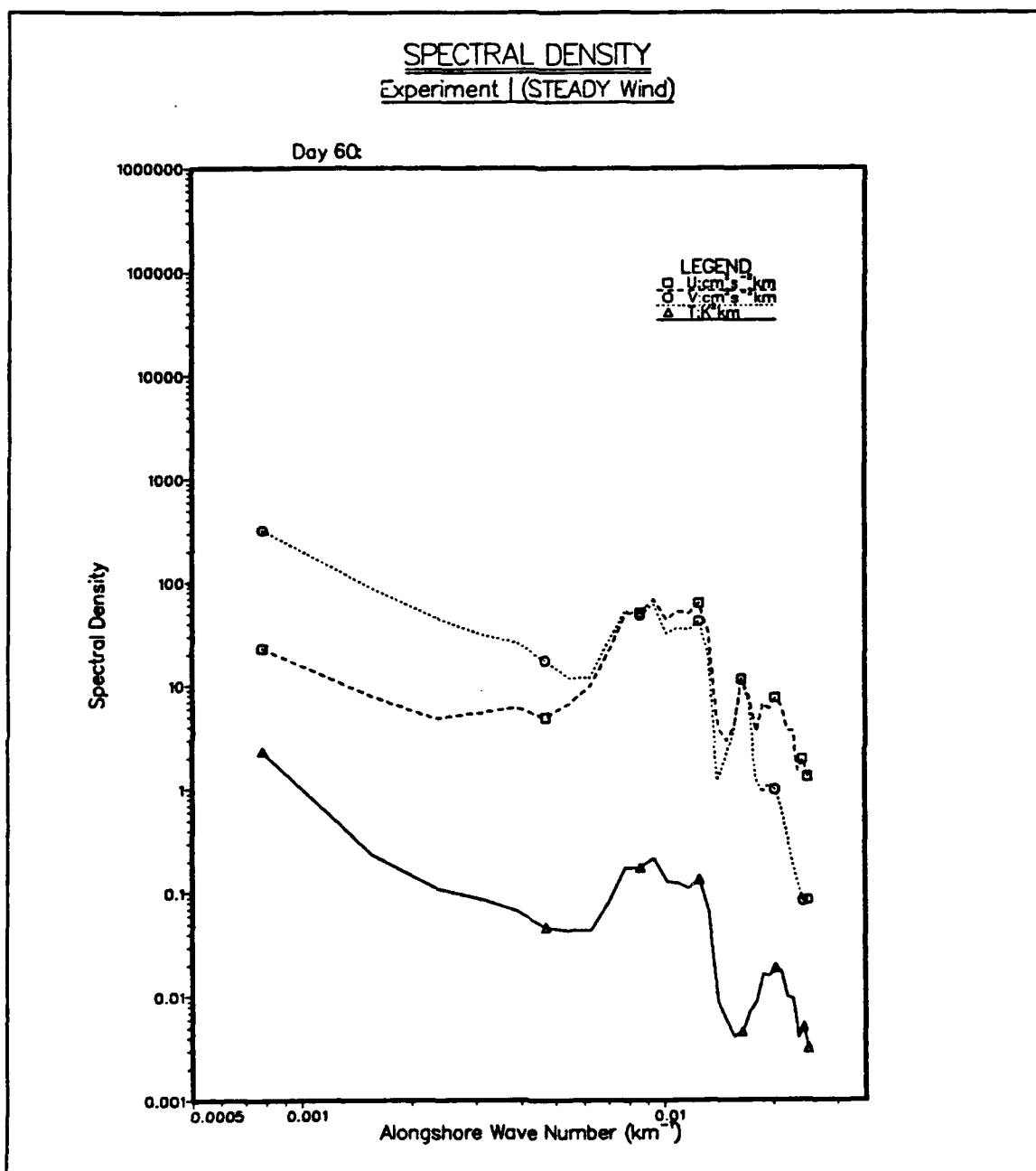


Figure 11. Spectral density at day 60 of Experiment 1: Dominant wavelength is $\sim 100 \text{ km}$, where $\lambda = \text{wavenumber}^{-1}$.

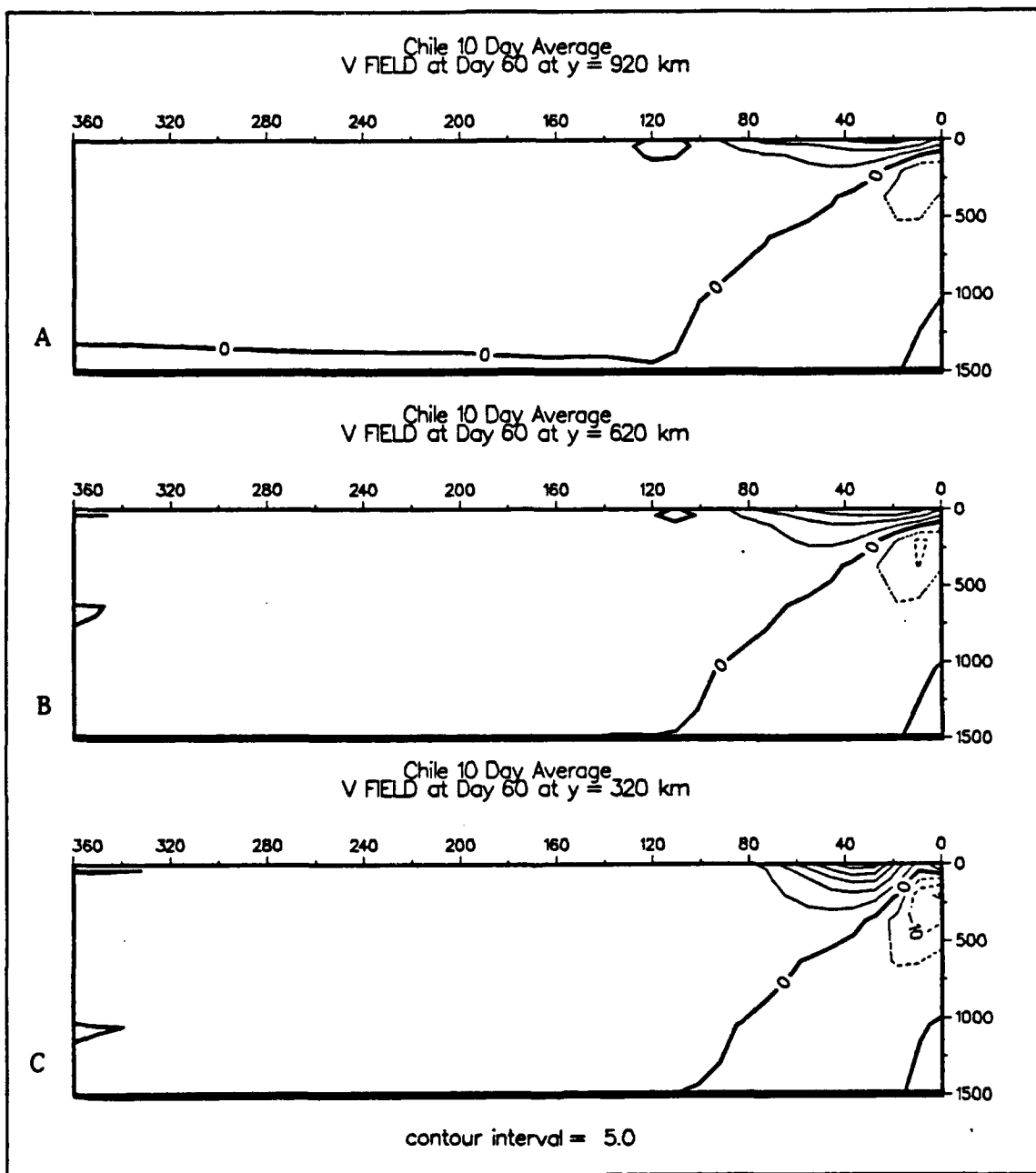


Figure 12. Zonal cross-sections of north-south velocity (V) at day 60 of Experiment 1: Velocities are in *cm/s*. Southward flowing currents are dashed.

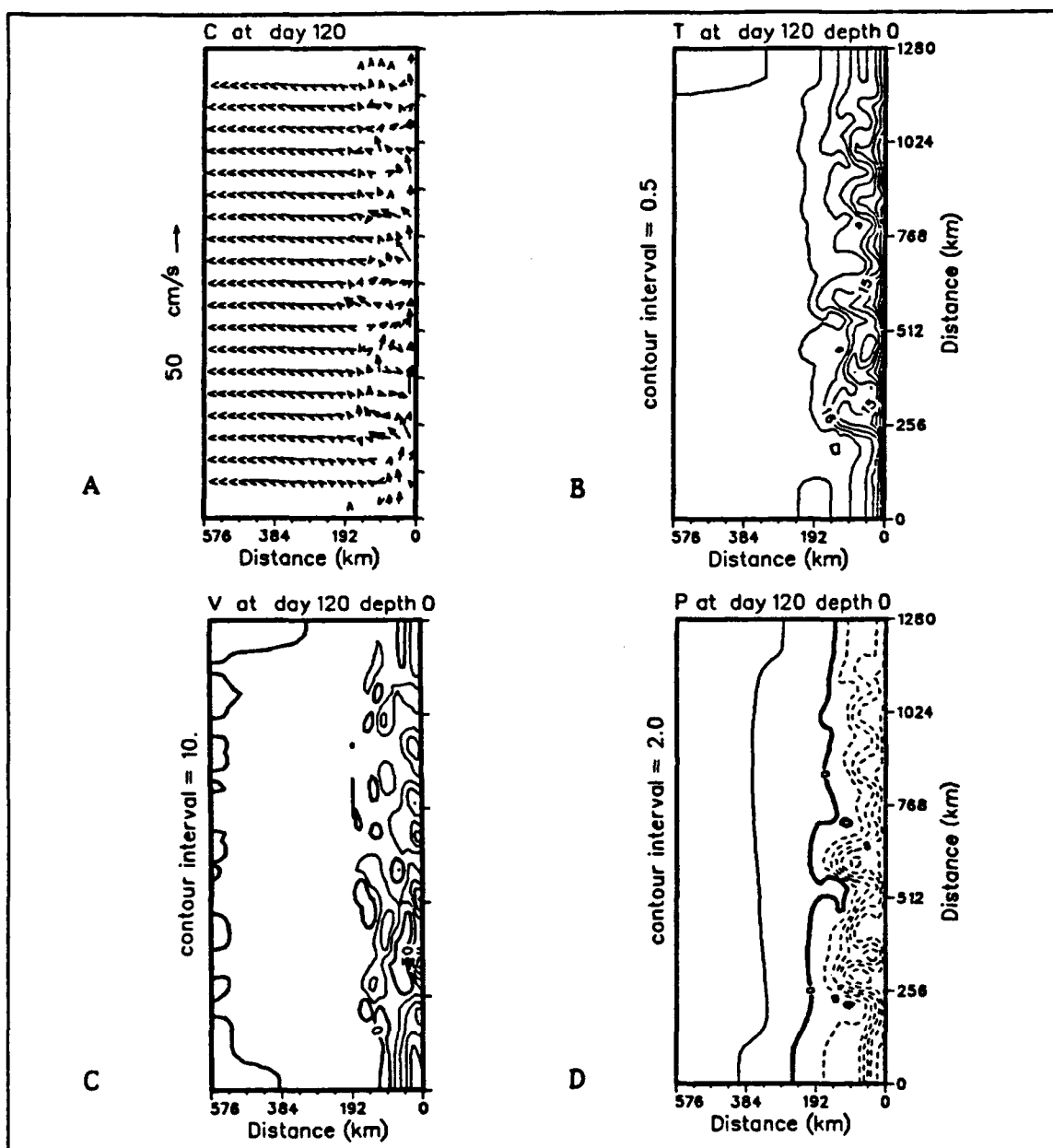


Figure 13. Surface current vectors, temperature, meridional velocity and dynamic height at day 120 of Experiment 1: Velocities are in *cm/s*, T is in $^{\circ}\text{C}$, heights are in *cm* relative to 2000 *m*. Dashed lines denote negative values.

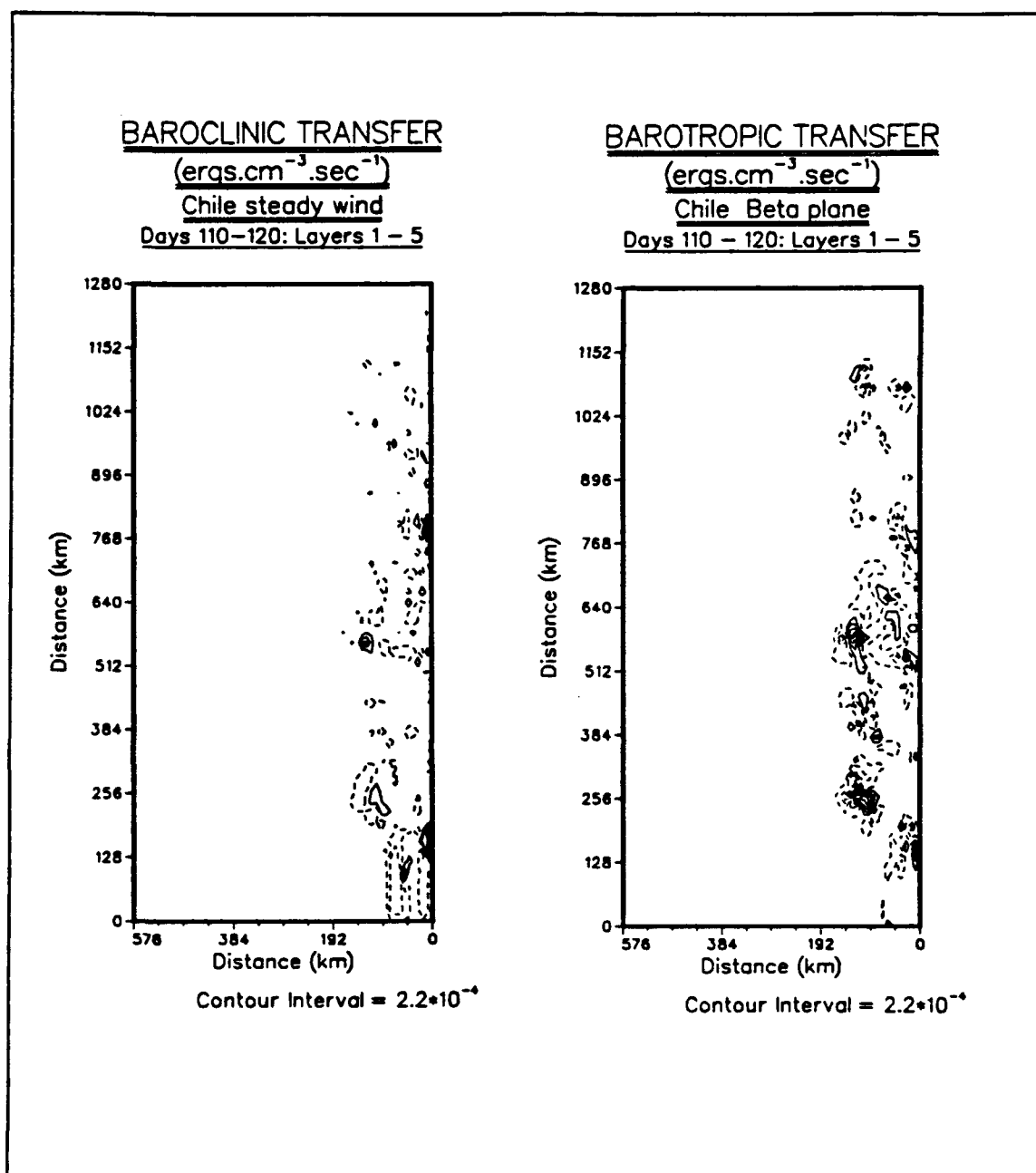


Figure 14. Baroclinic and barotropic instability at day 120 of Experiment 1

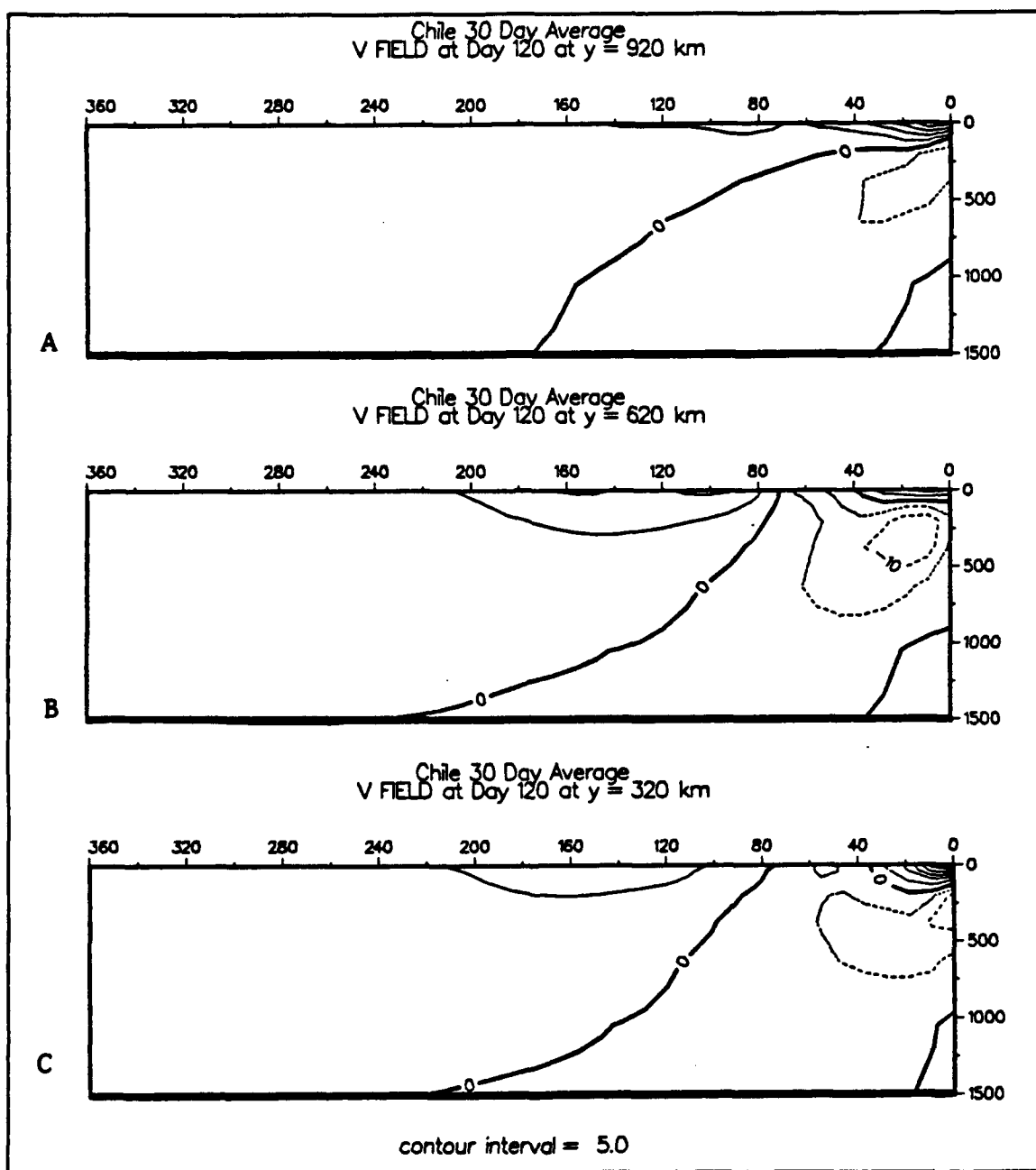


Figure 15. Zonal cross-sections of north-south velocity (V) at day 120 of Experiment 1: Velocities are in *cm/s*. Southward flowing currents are dashed.

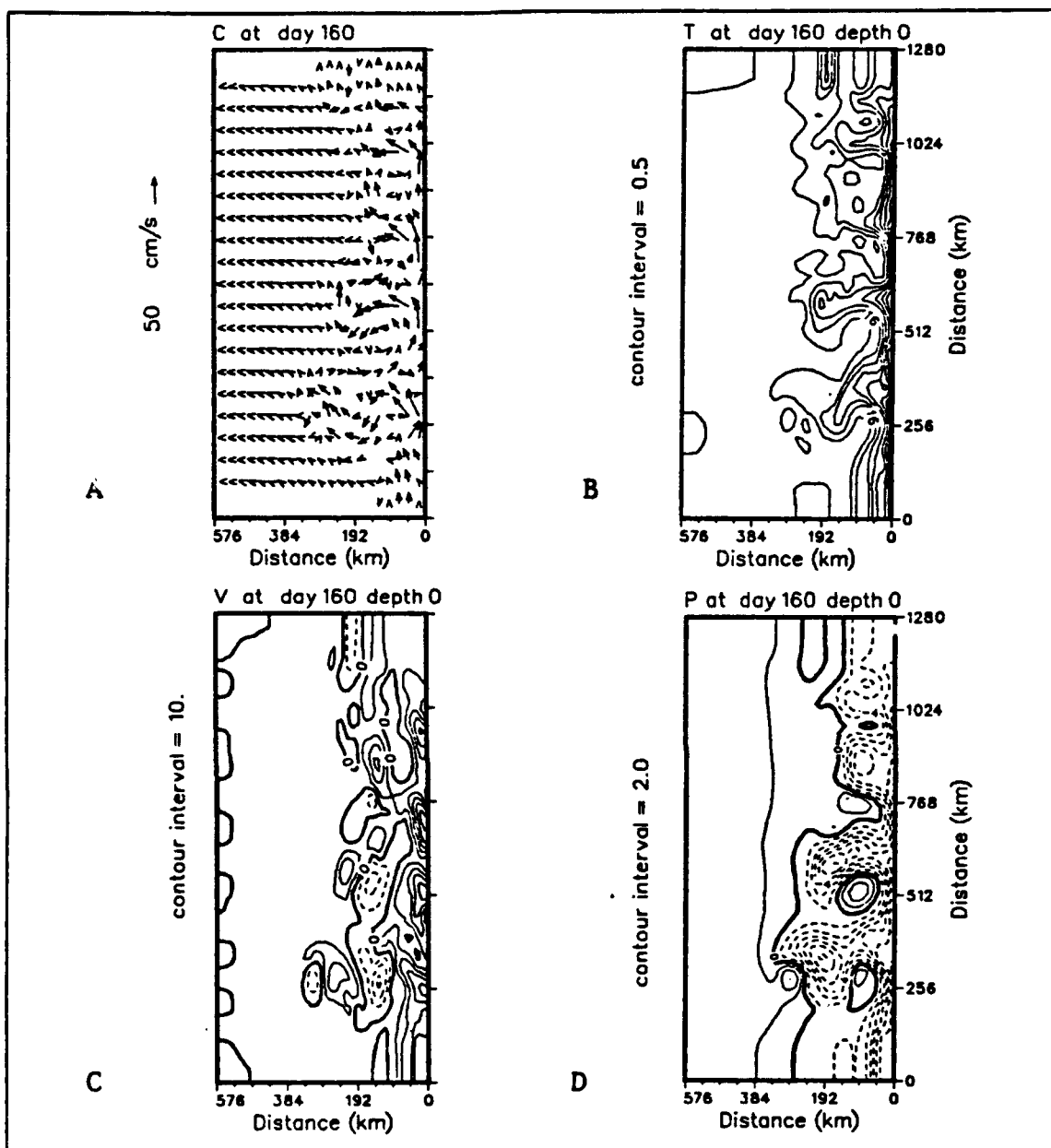


Figure 16. Surface current vectors, temperature, meridional velocity and dynamic height at day 160 of Experiment 1: Velocities are in cm/s , T is in $^{\circ}C$, heights are in cm relative to 2000 m . Dashed lines are southward velocities (C) or negative values (D).

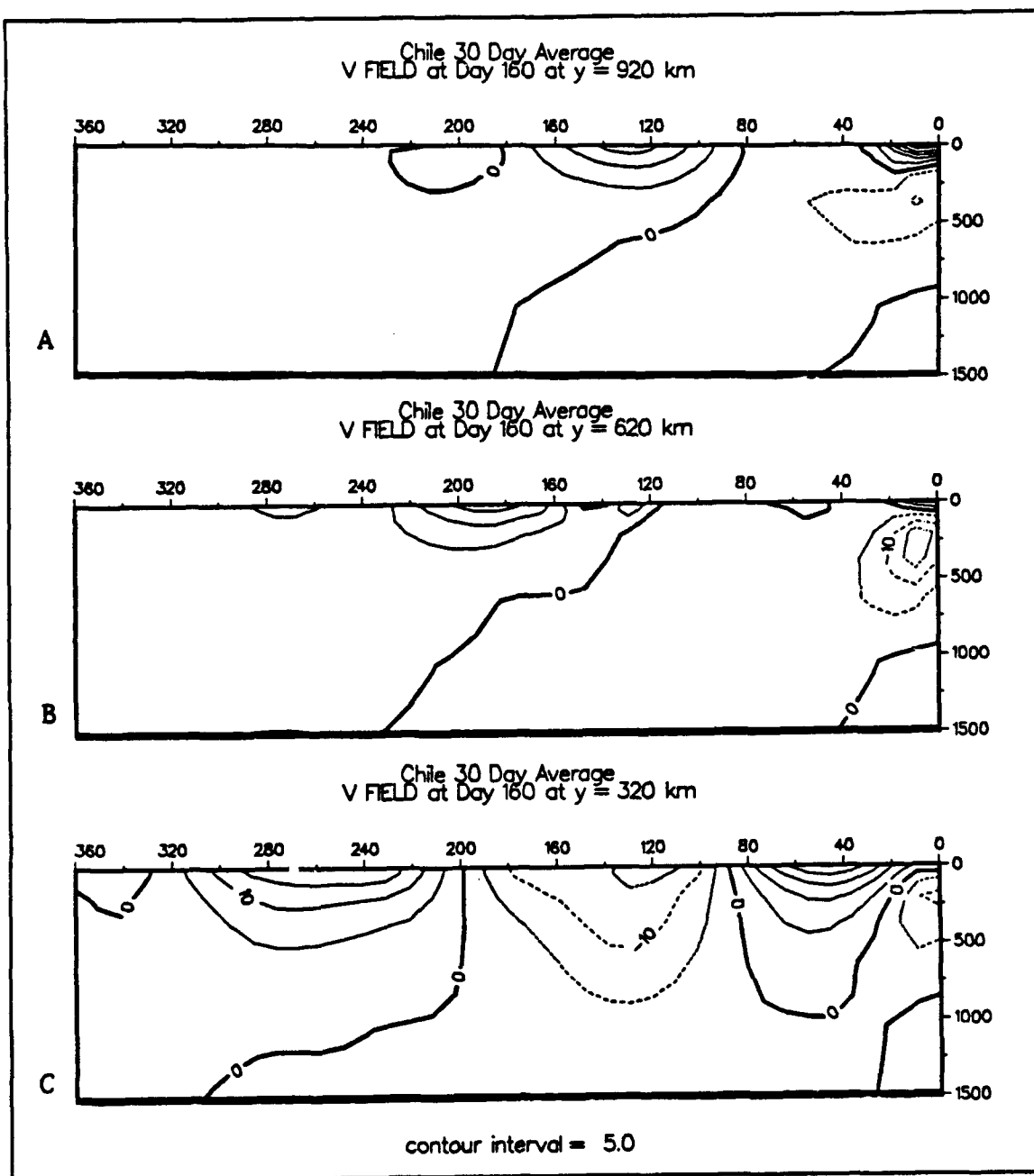


Figure 17. Zonal cross-sections of north-south velocity (V) at day 160 of Experiment 1: Velocities are in *cm/s*. Southward flowing currents are dashed.

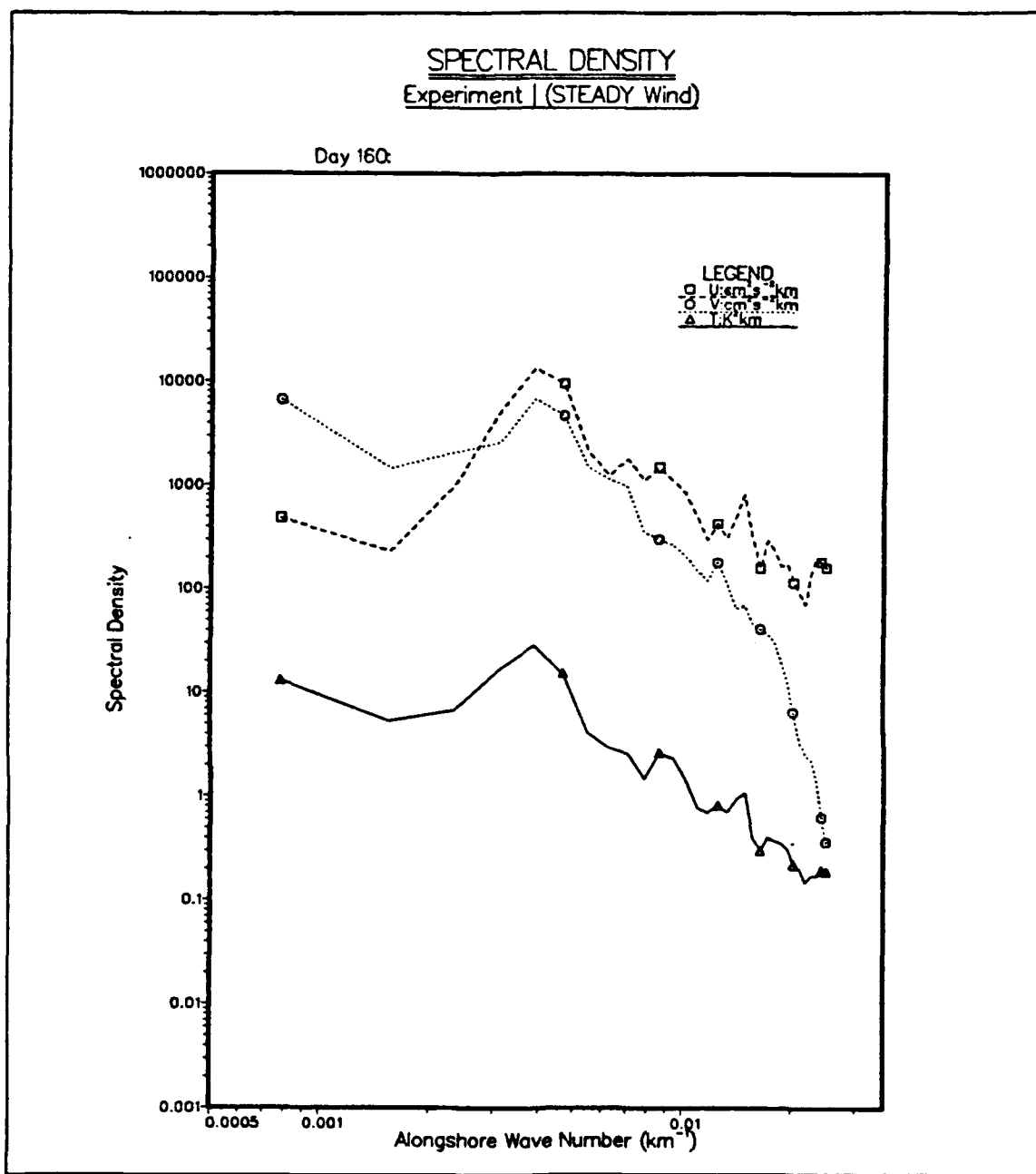


Figure 18. Spectral density at day 160 of Experiment 1: Dominant wavelength is $\sim 250 \text{ km}$.

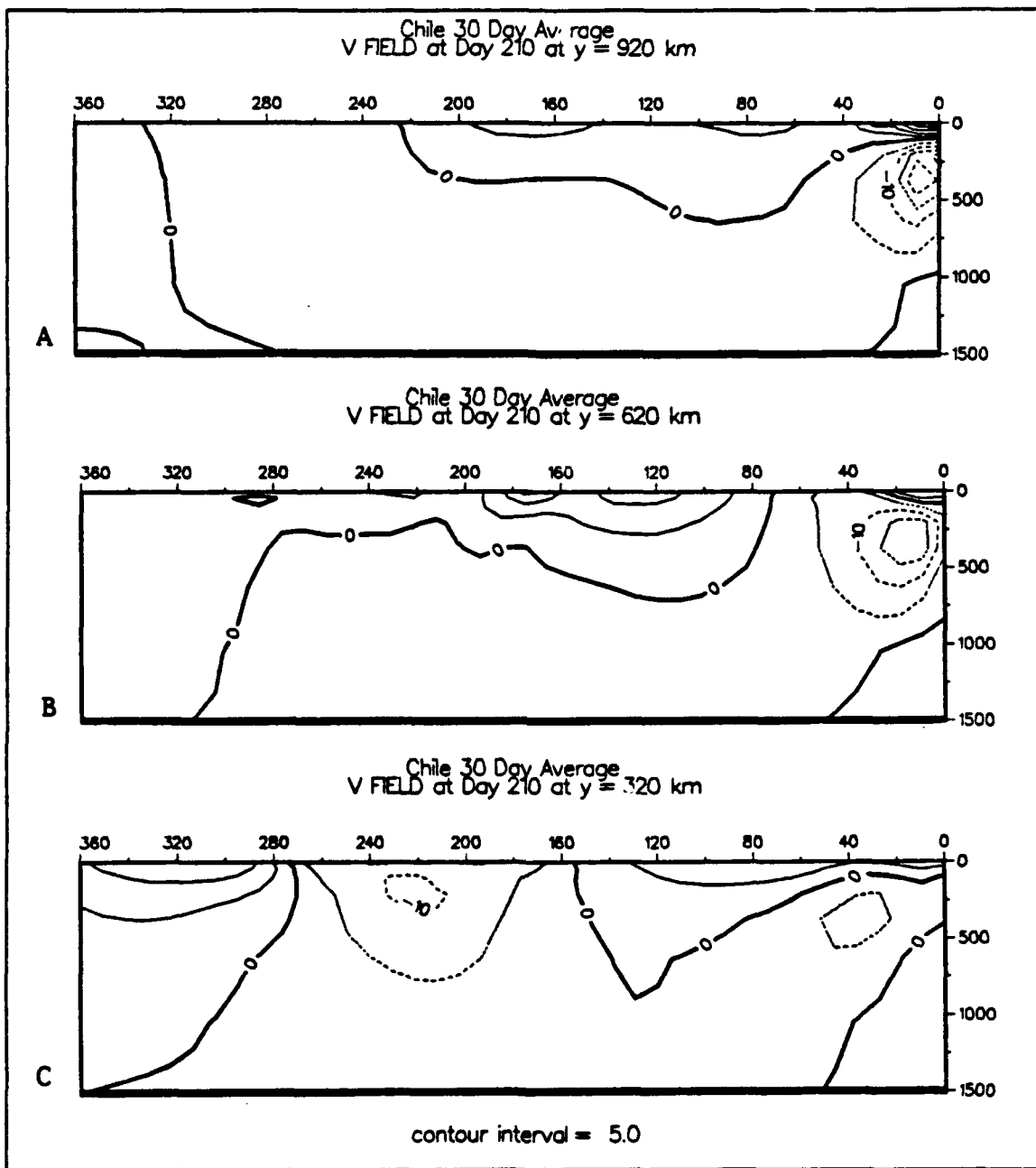


Figure 19. Zonal cross-sections of north-south velocity (V) at day 160 of Experiment 1: Velocities are in *cm/s*. Southward flowing currents are dashed.

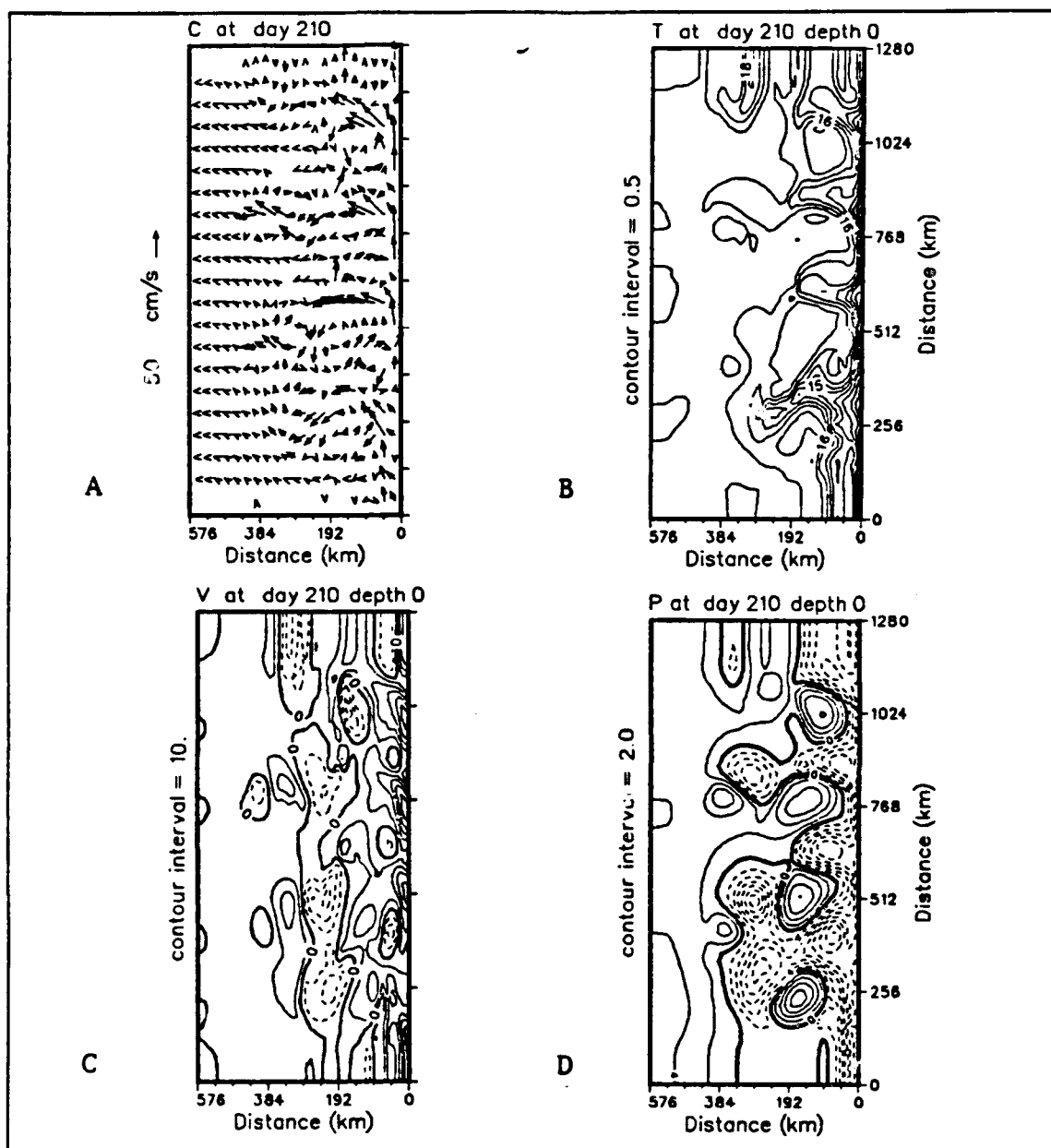


Figure 20. Surface current vectors, temperature, meridional velocity and dynamic height at day 210 of Experiment 1: Velocities are in cm/s , T is in $^{\circ}C$, heights are in cm relative to 2000 m . Dashed lines are southward velocities (C) or negative values (D).

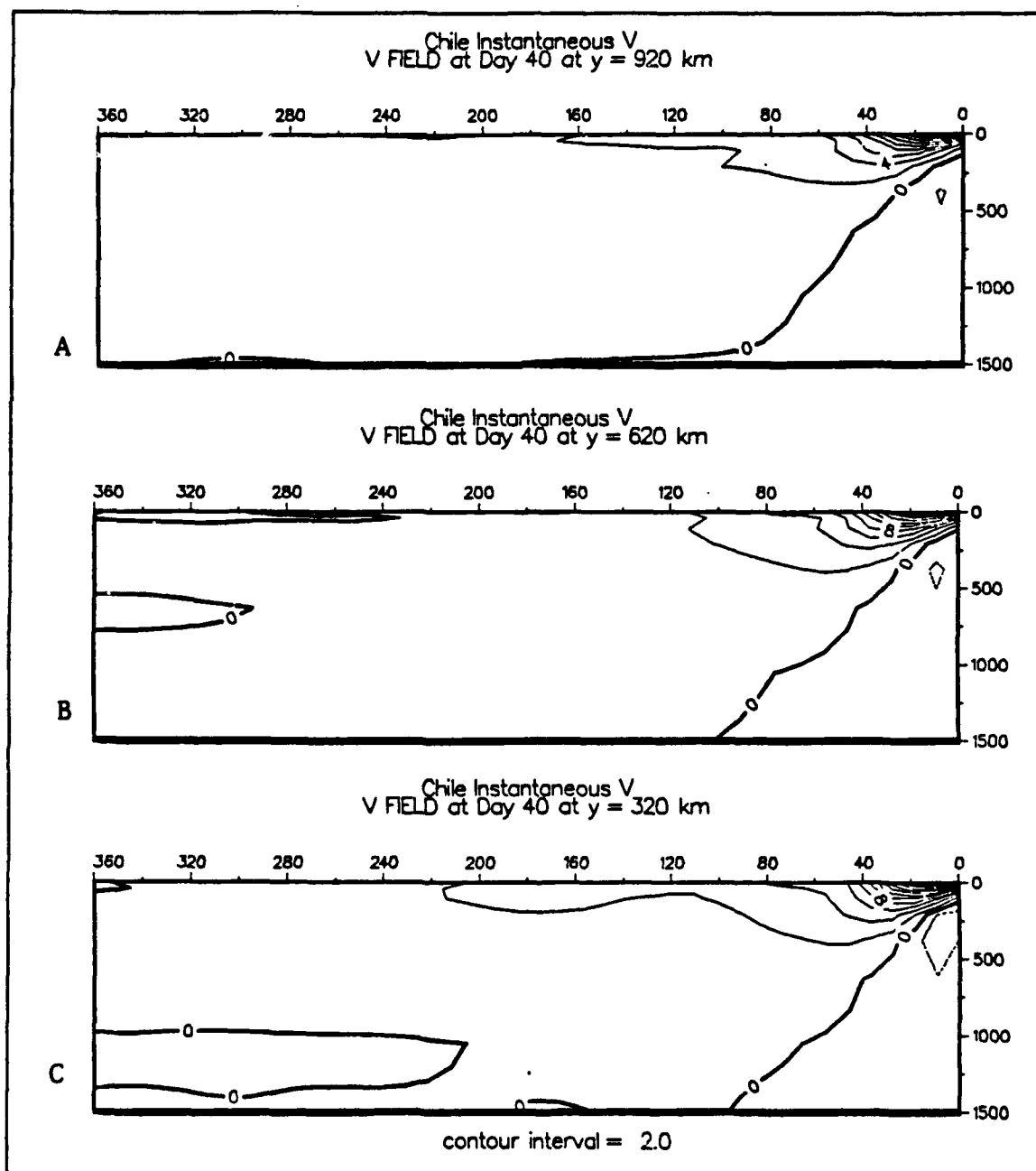


Figure 21. Zonal cross-sections of north-south velocity (V) at day 40 of Experiment 2: Velocities are in *cm/s*. Southward flowing currents are dashed.

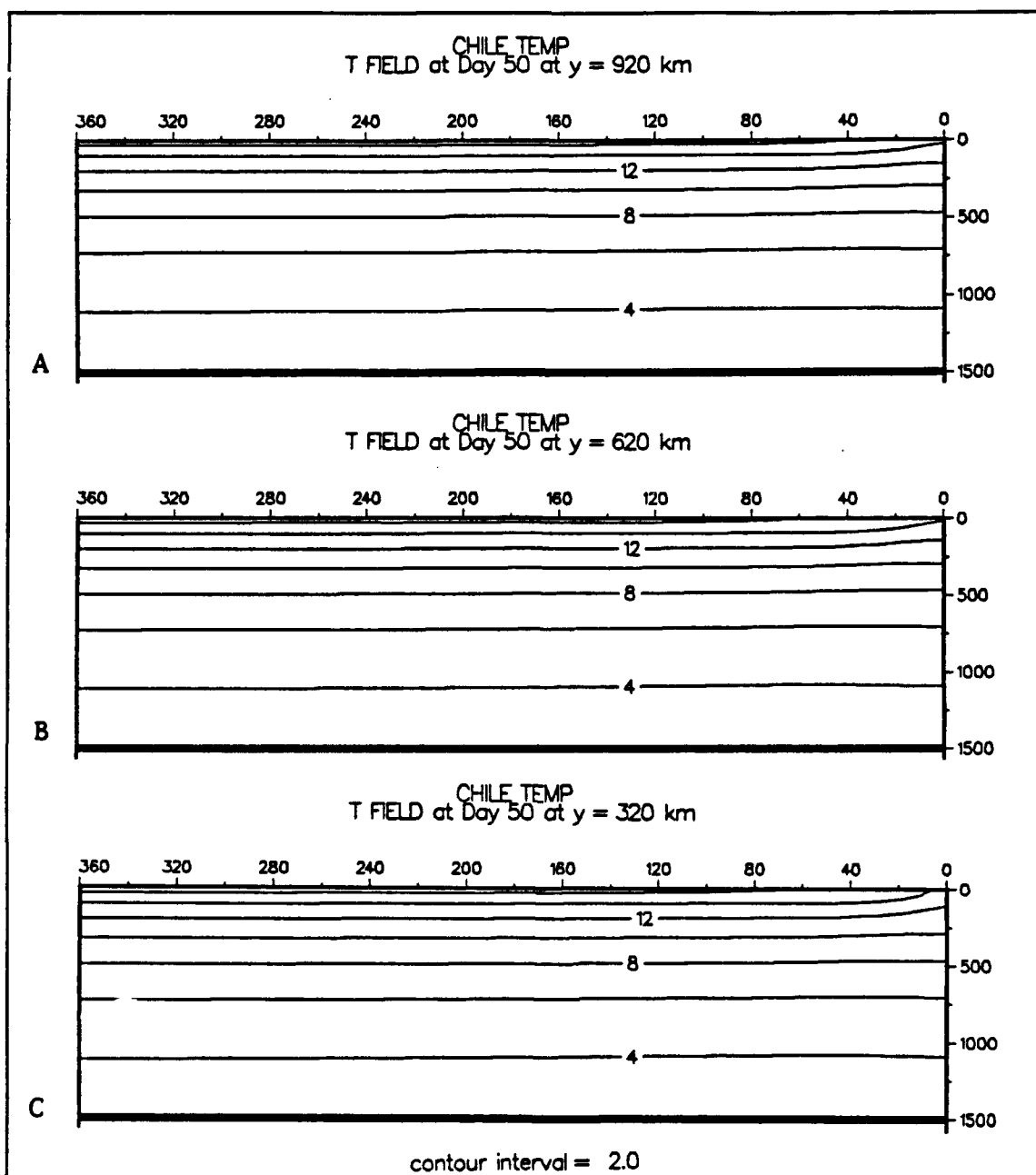


Figure 22. Zonal cross-sections of north-south temperature (T) at day 50: Temperatures are in °C.

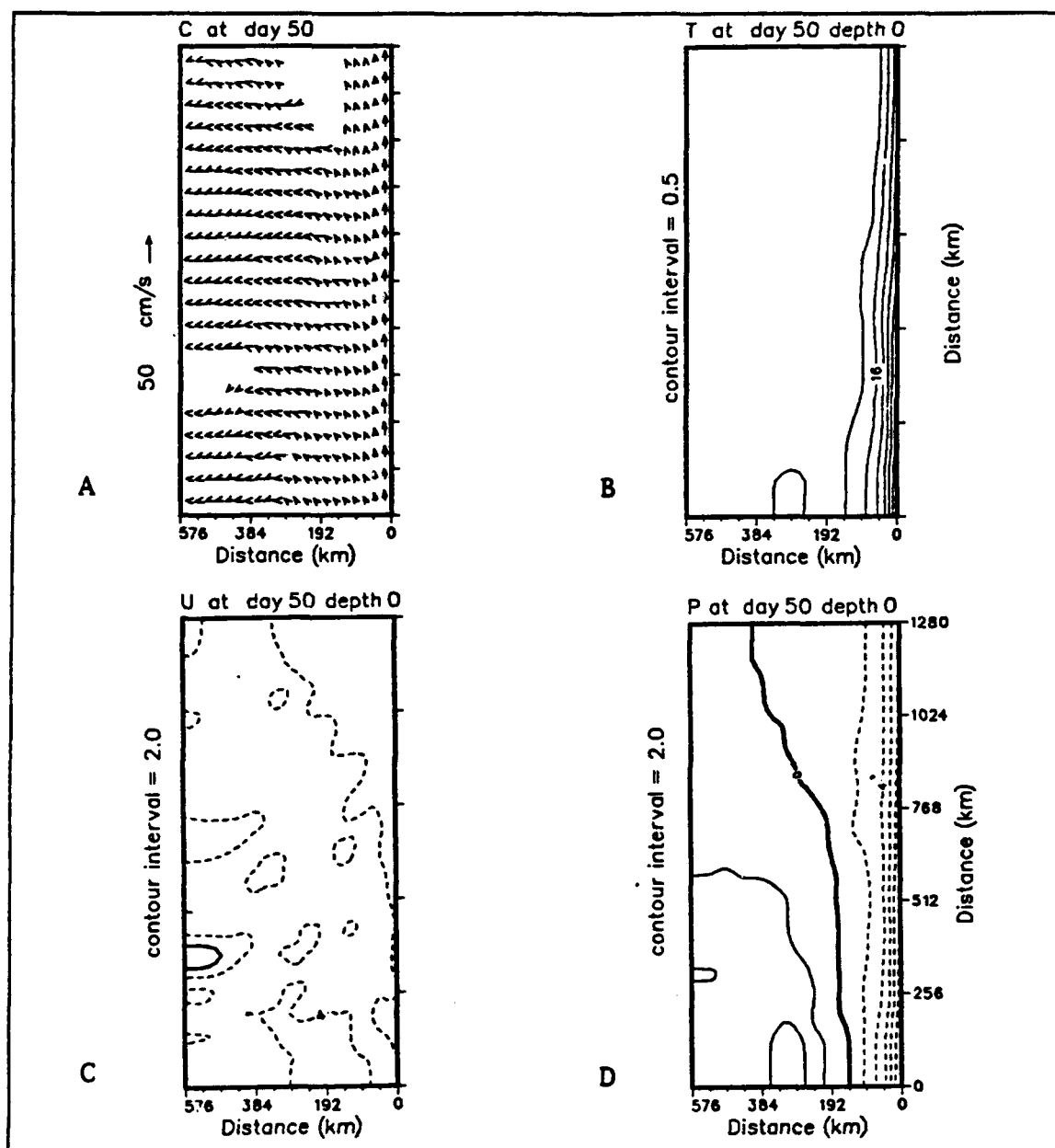


Figure 23. Surface current vectors, temperature, zonal velocity and dynamic height at day 50 of Experiment 2: Velocities are in cm/s , T is in $^{\circ}C$, heights are in cm relative to 2000 m . Dashed lines are westward velocities (C) or negative values (D).

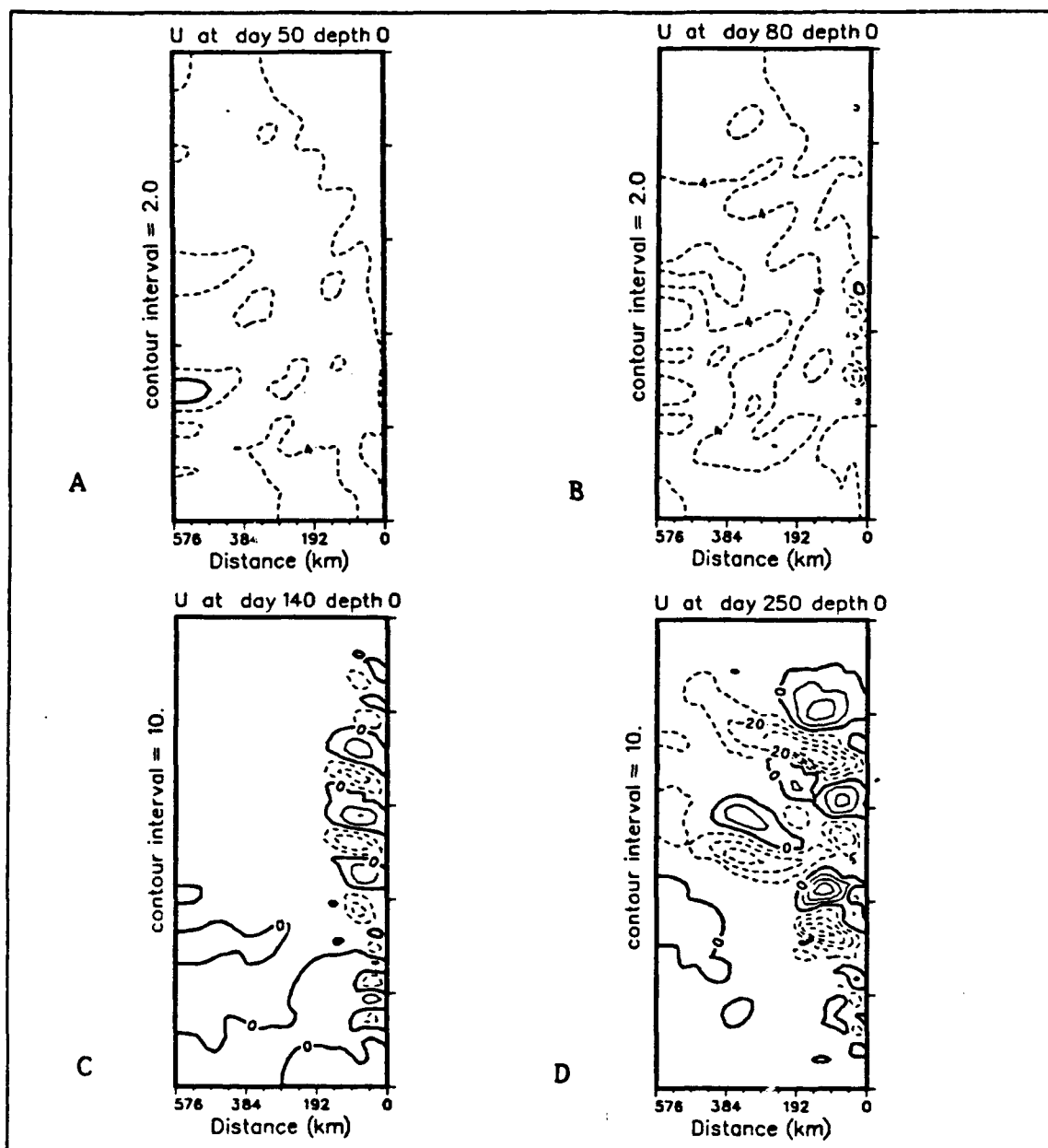


Figure 24. Surface zonal velocity (U) for Experiment 2: Velocities are in *cm/s*.
Dashed lines are westward velocities.

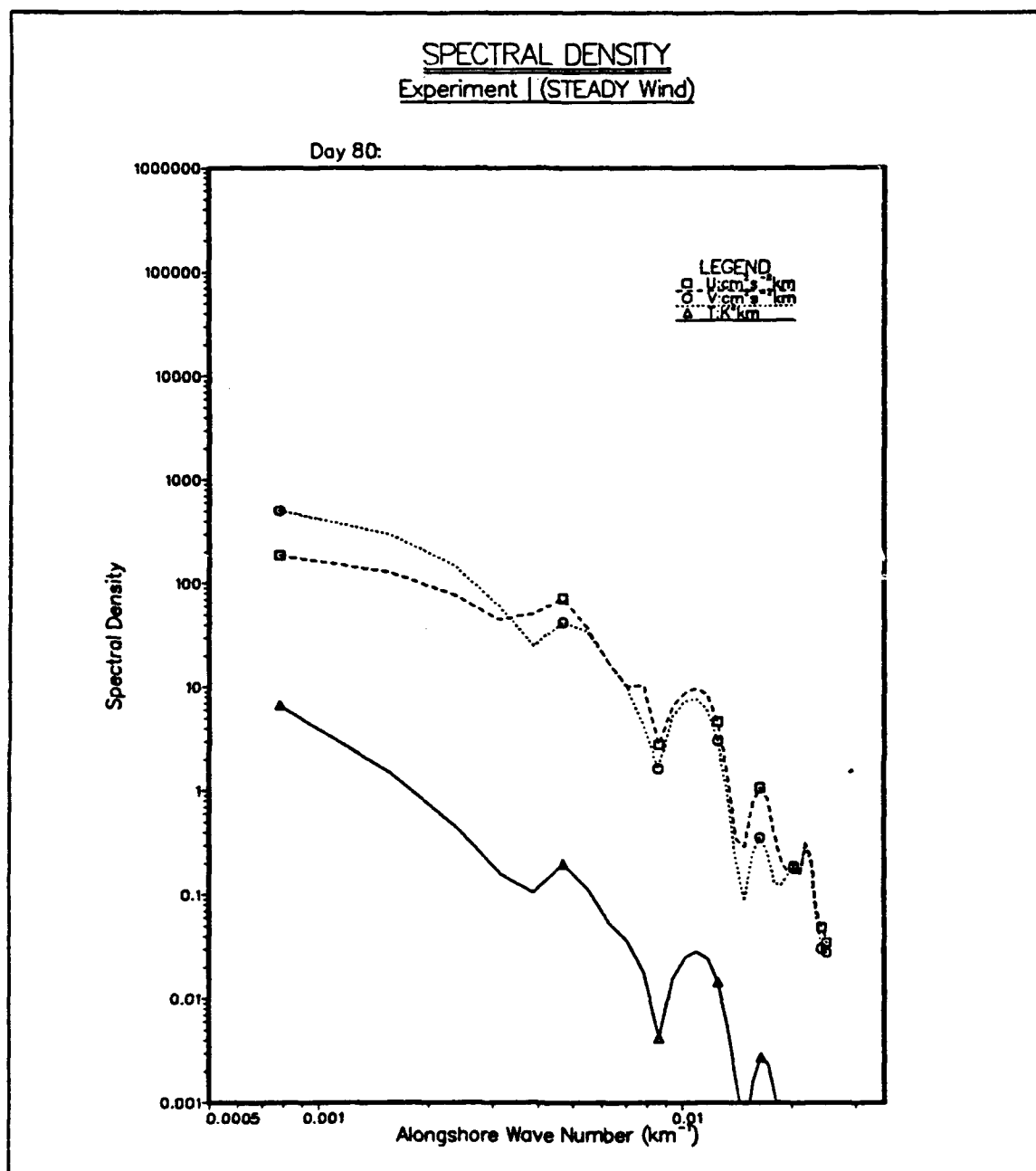


Figure 25. Spectral Density at day 80 of Experiment 2: Dominant wavelength is $\sim 250 \text{ km}$, with a secondary wavelength evident at $\sim 85 \text{ km}$.

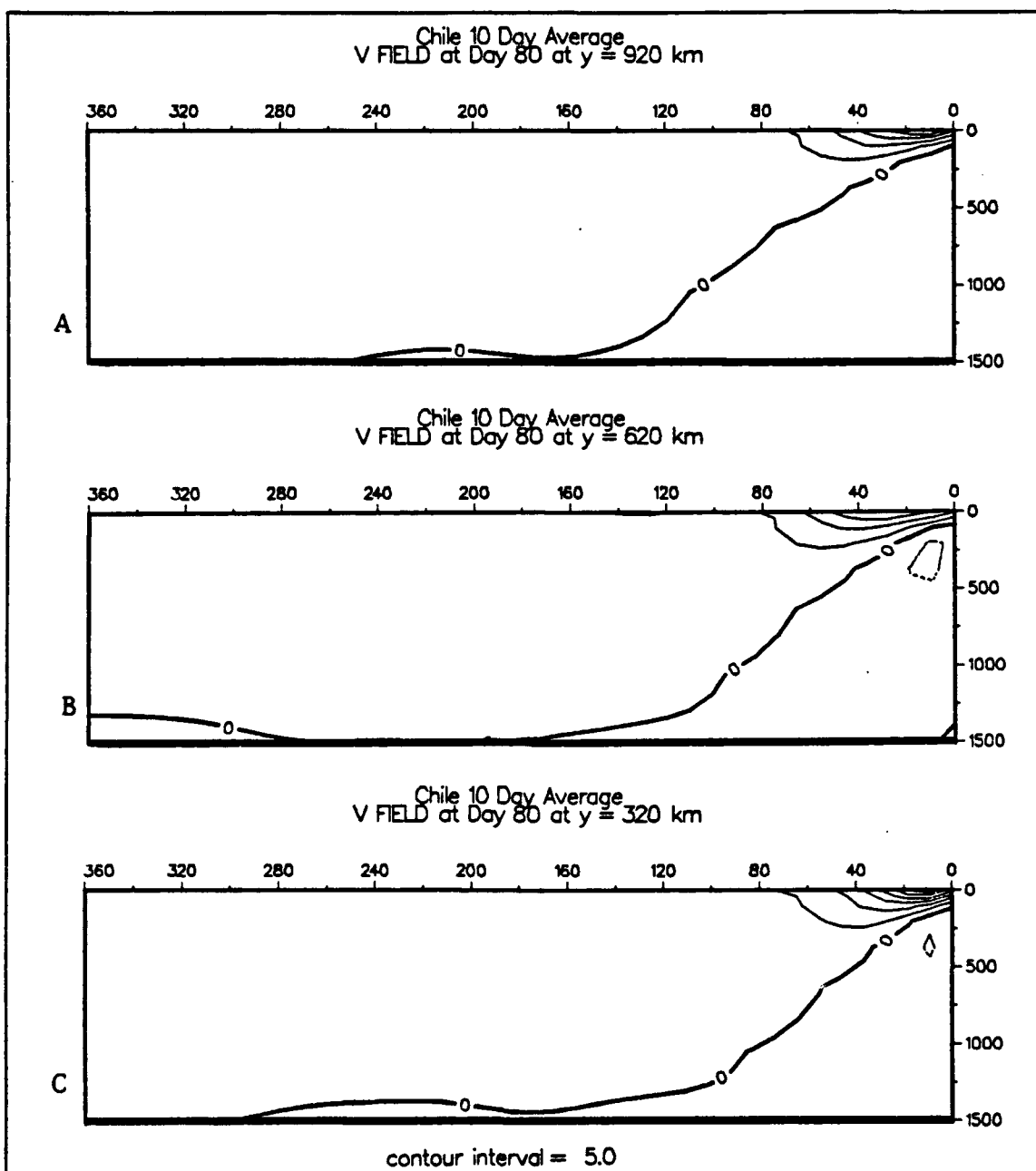


Figure 26. Zonal cross-sections of north-south velocity (V) at day 80 of Experiment 2: Velocities are in *cm/s*. Southward flowing currents are dashed.

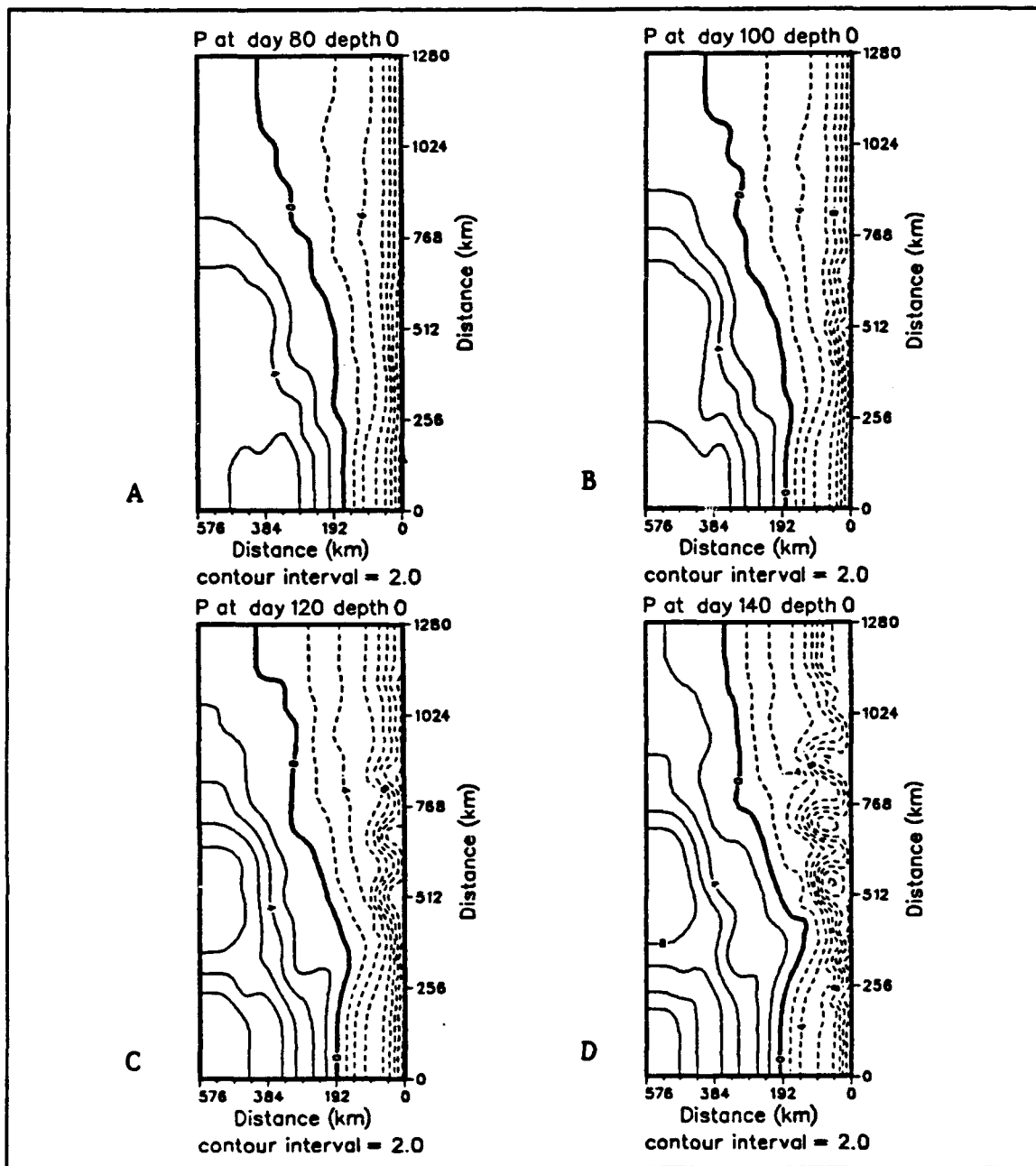


Figure 27. Dynamic height, days 80-140 of Experiment 2: Heights are in *cm* relative to 2000 *m*. Dashed lines denote negative height values.

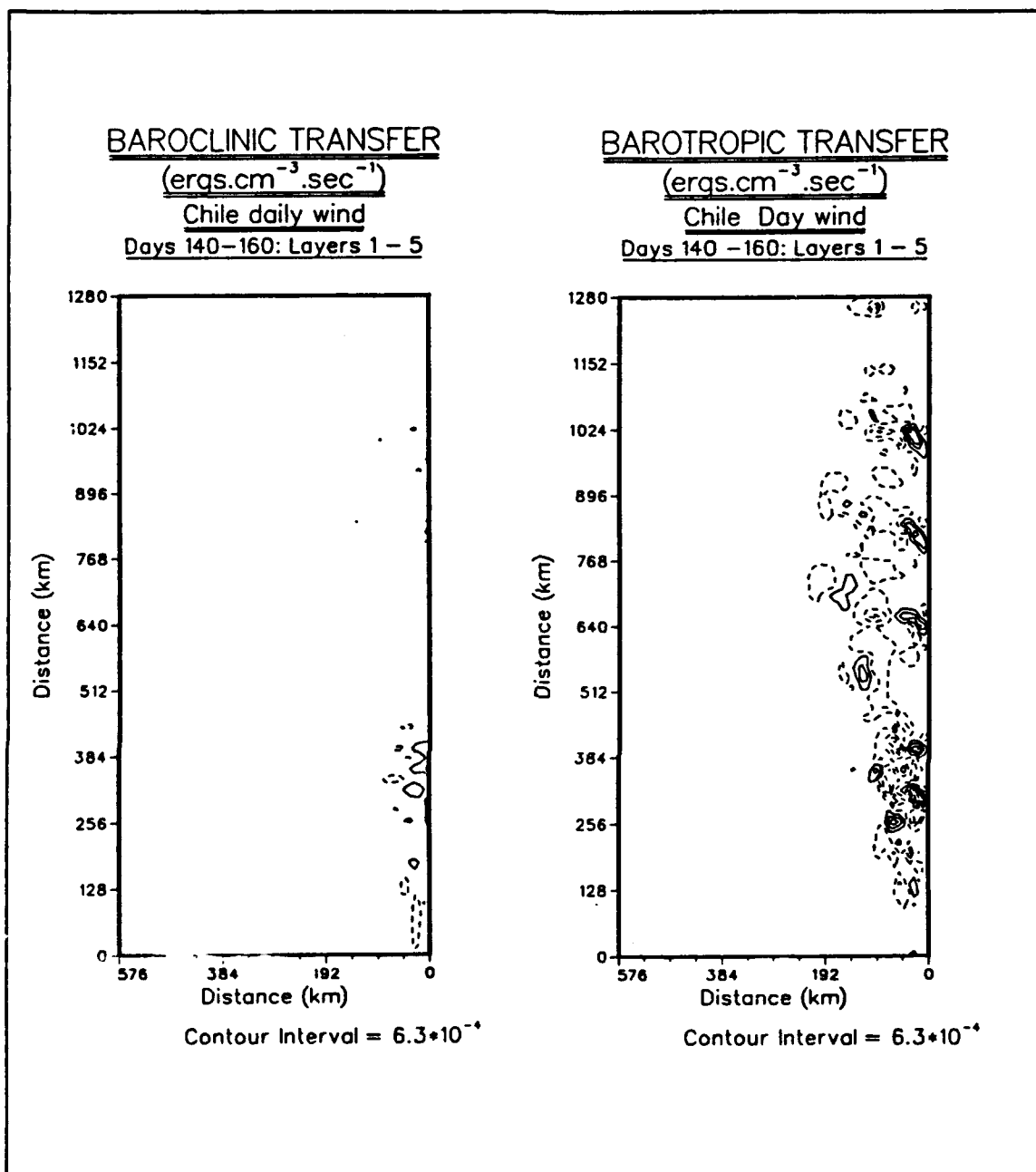


Figure 28. Baroclinic and barotropic instability at day 140 of Experiment 2.

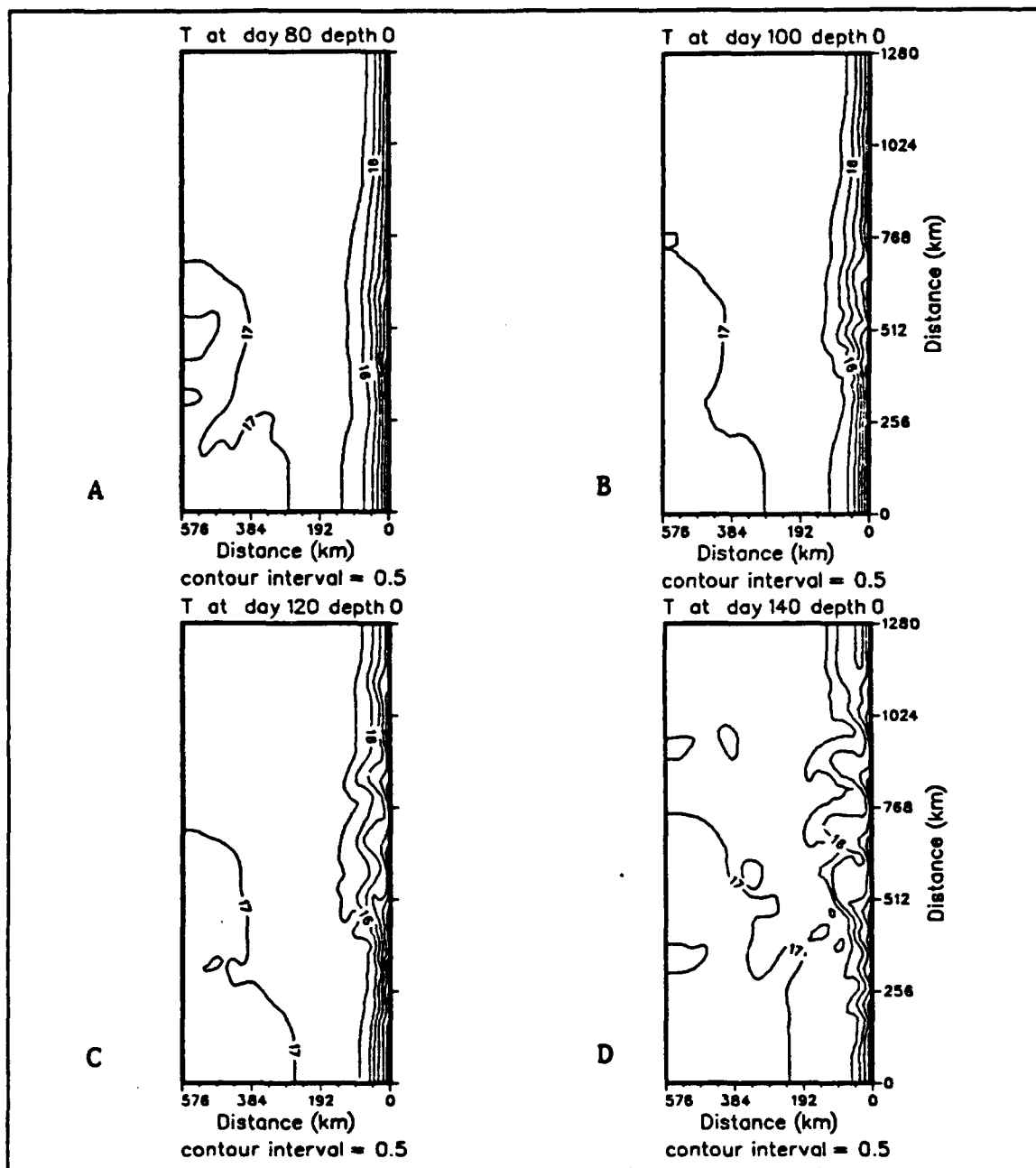


Figure 29. Surface temperature contours for Experiment 2: Temperatures are in °C. Temperature bands in the south are narrower during the austral fall.

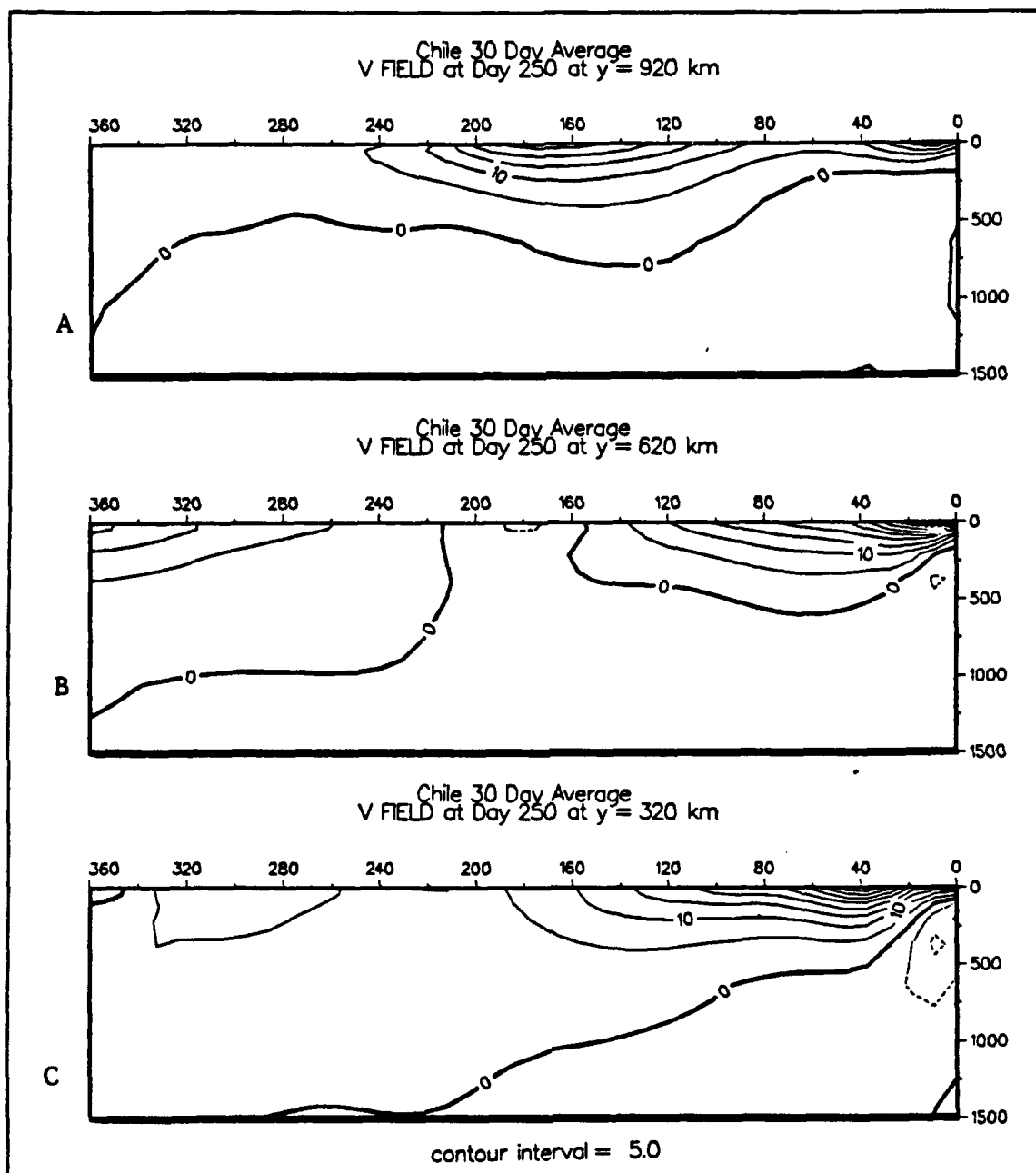


Figure 30. Zonal cross-sections of north-south velocity (V) at day 250 of Experiment 2: Velocities are in *cm/s*. Southward flowing currents are dashed.

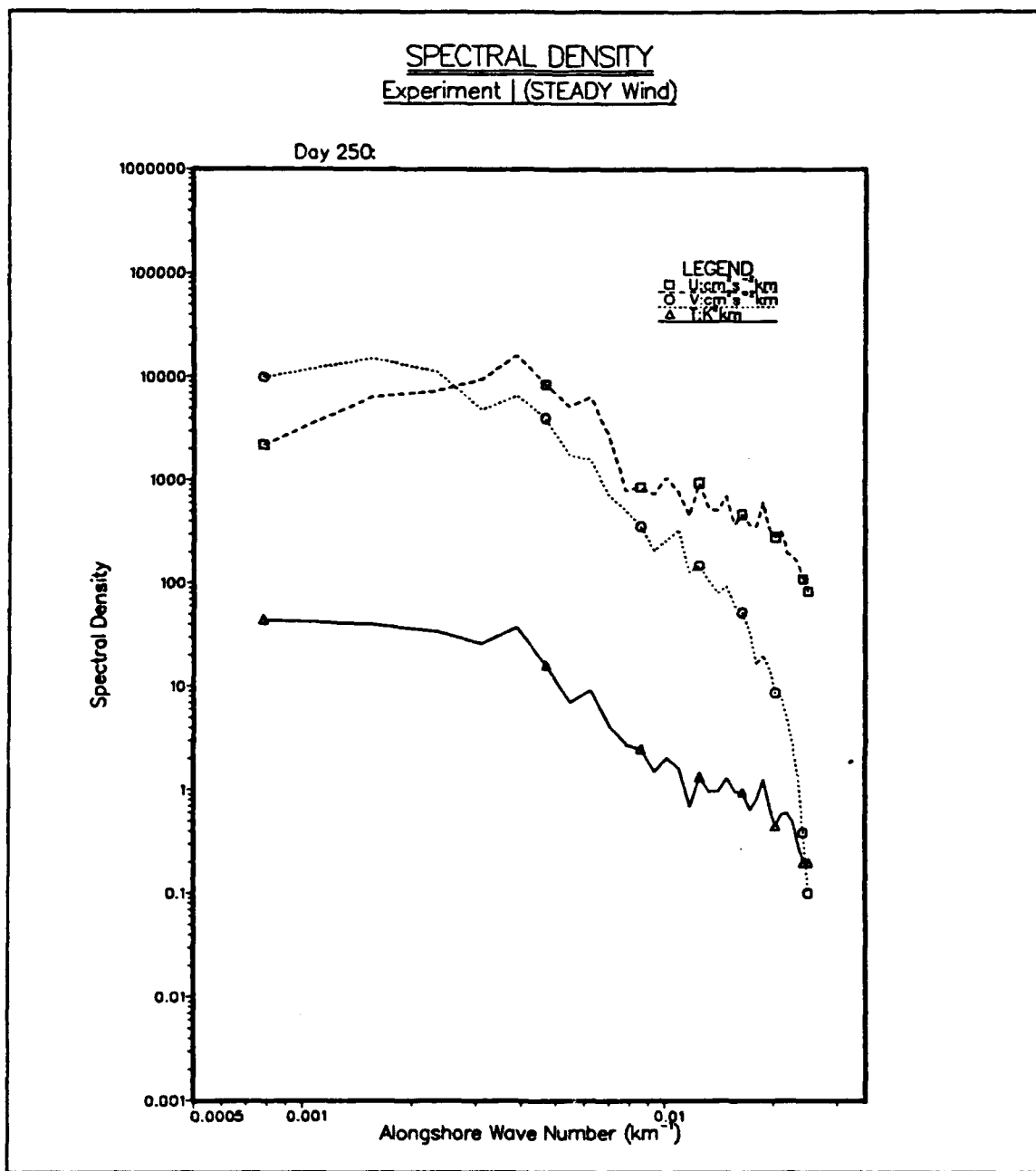


Figure 31. Spectral density at day 250 of Experiment 2: Dominant wavelength is $\sim 250 \text{ km}$, with a secondary wavelength evident at $\sim 85 \text{ km}$.

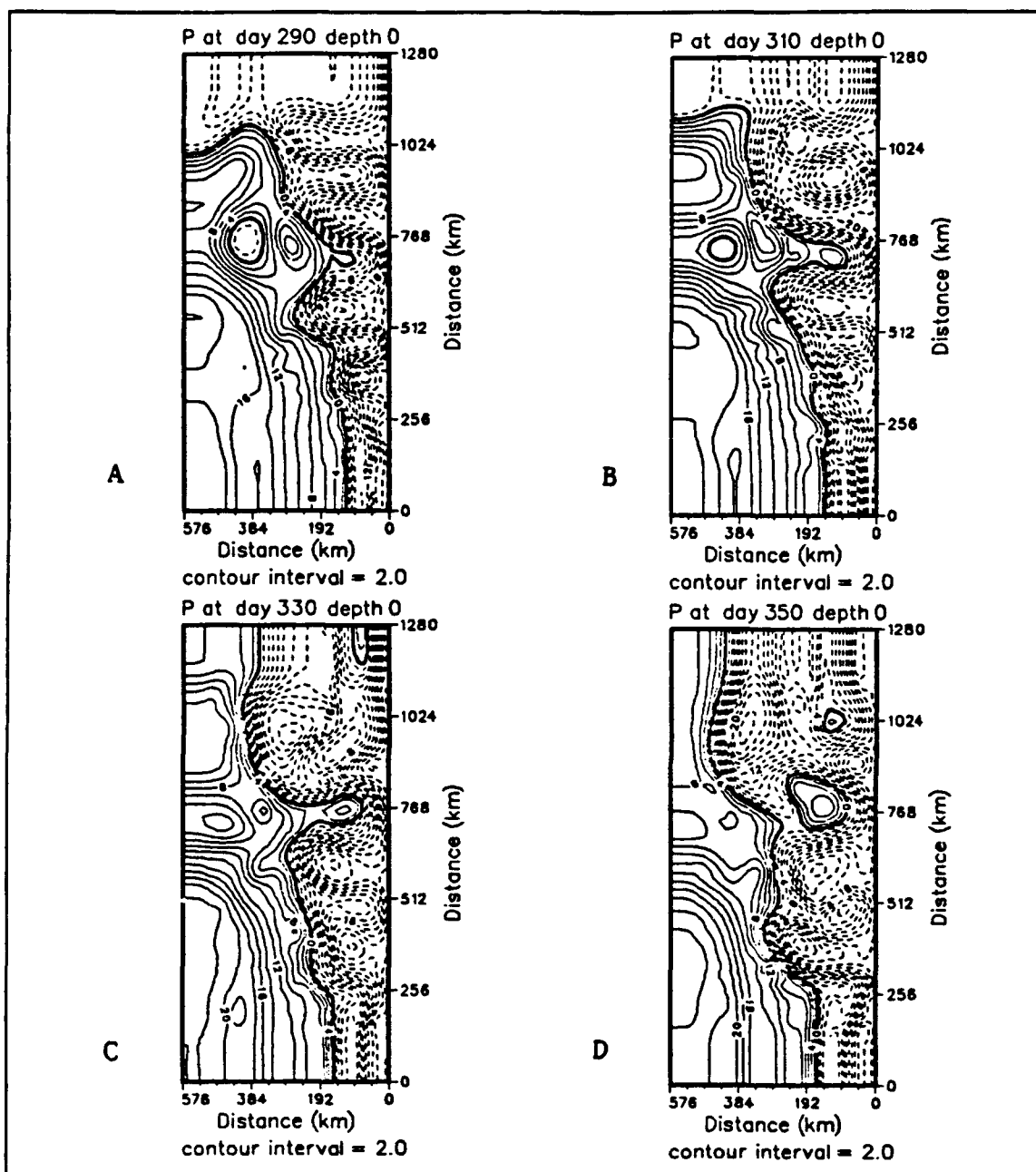


Figure 33. Dynamic height, days 290-350 of Experiment 2: Heights are in *cm* relative to 2000 *m*. Dashed lines denote negative height values.

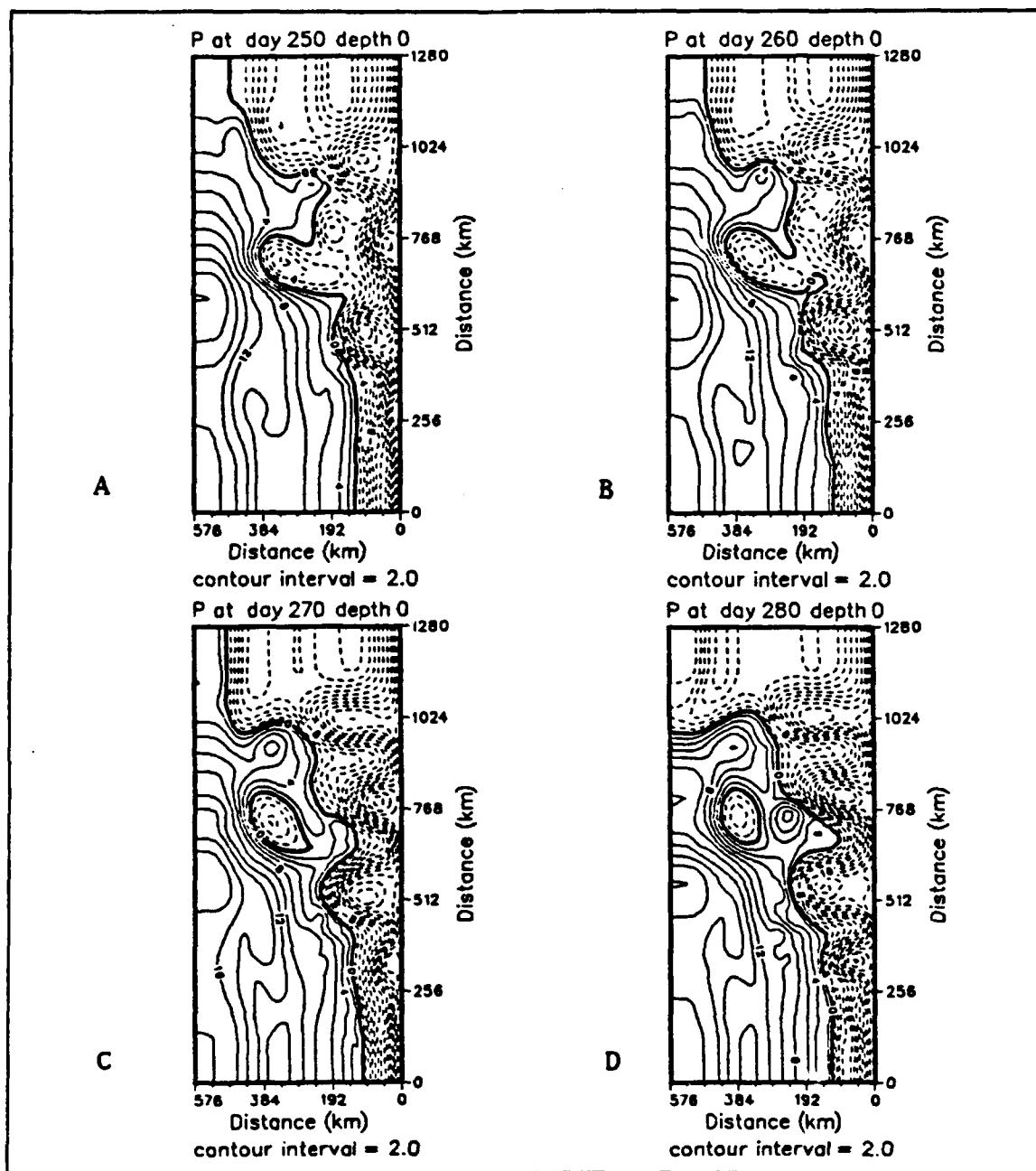


Figure 32. Dynamic height, days 250-280 of Experiment 2: Heights are in *cm* relative to 2000 *m*. Dashed lines denote negative height values.

VI. SUMMARY AND RECOMMENDATIONS

A. SUMMARY

This study used a high-resolution, primitive equation numerical model to study the effects of steady and daily varying winds on the Chile Current System. The model domain was a rectangular region extending 6° off the coast, between 22° and 34° S.

In Experiment 1, a constant wind stress was applied to the model domain, excluding the northern and southern open boundaries, for a period of 240 days. The objective was to simulate the generally equatorward-flowing winds that are seen in that part of the world, for most of the year. Both an equatorward-flowing surface current and a poleward-flowing undercurrent developed. Average surface equatorward and subsurface poleward velocities were $\sim 25 - 30$ cm/s. Eddies formed in the southern part of the domain first, then spread north and south, eventually dominating the coastal region. The dominant wavelength for the eddies was ~ 250 km.

In Experiment 2, temporally and spatially interpolated values of monthly climatological winds were used as the forcing for the model. Unlike Experiment 1, the varying winds allowed the following processes to be studied. First, it allowed the study of the effects of seasonal wind variations on the behavior of the current system. Second, it allowed the influence of wind stress curl on coastal dynamics to be investigated. Third, it introduced the zonal component of the wind stress, allowing the study of the oceanic response to this additional component of stress.

Initially, when winds were generally equatorward, the two models were similar, with the development of coastal currents and upwelling along the coast. As the seasonal regime of the winds changed, differences, as expected, were discernible. For example, the poleward-flowing undercurrent in Experiment 2 was slower to develop, especially in the

northern parts of the region. The surface equatorward current reached a maximum speed of $> 50 \text{ cm/s}$ in Experiment 2 compared to a maximum speed of $\sim 30 \text{ cm/s}$ in Experiment 1. The average undercurrent in Experiment 2 was $\sim 15 \text{ cm/s}$, which is slower than in Experiment 1 (which had velocities of $\sim 25 \text{ cm/s}$). In Experiment 2, the undercurrent was centered at $\sim 300 \text{ m}$ depth, compared to $\sim 250 \text{ m}$ in Experiment 1. In Experiment 2, instabilities did not appear until day 80, a full 30 days later than in Experiment 1. Baroclinic instability played a smaller role (than in Experiment 1) in the creation of eddies, except in the extreme southern part of the region. Once eddies did form, however, their sizes varied with latitude and time, tending to grow larger in the north where the winds were usually mostly meridional, and virtually disappearing in the south, when the alongshore wind stress was at a minimum. These southern eddies began to grow again, however, once stronger winds returned to the region. In the north, the dominant wavelength was $\sim 250 \text{ km}$, while in the south it was $\sim 85 \text{ km}$.

B. RECOMMENDATIONS

Of critical importance to any process-oriented study is the comparison of model output with available observations. Without such comparisons, model studies are difficult to verify, and become speculative in nature. As mentioned by several authors (e.g., Fonseca, 1989; Bakun and Nelson, 1991), the waters off the coast of Chile are notoriously lacking in both wind and current data, and until more observational studies are conducted, the Chile Current System will remain somewhat of a mystery. Johnson (1989) suggests that satellite imagery of the South American coastal waters may provide the most readily obtainable basis for increasing the number of available observations. Much of the model output from numerical simulations could then be compared directly to the imagery. Figure 34A shows a satellite image from Fonseca (1989) of a cold filament extending out $\sim 40 \text{ km}$ off the coast of Chile, near 33° S , while Figure 34B shows the surface temperature field at day 290 of the Experiment 2 model run, in which cold

filaments can be seen extending to the west. The 14° contour at several locations protrudes 40-60 *km* from the coast, a distance very similar to that seen in satellite imagery. Comparison of the two figures suggests that the model results may have some validity, although many more comparisons would need to be made before such a claim could be made with any certainty. This merging of model output and real-time satellite verification may well be the next logical step in understanding the Chilean coastal waters, and is a recommended area of future study, as such observations (e. g., GEOSAT, SEASAT) become available.

The knowledge gained in this investigation can benefit Naval Oceanography by providing a basis for prediction not only in the Chilean Current System, but also in other dynamically similar Eastern Boundary Current regions. An understanding of the formation and evolution of eddy and jet structures is an essential step in the development of a real-time analysis and prediction capability for these important features (Robinson *et al.*, 1984).

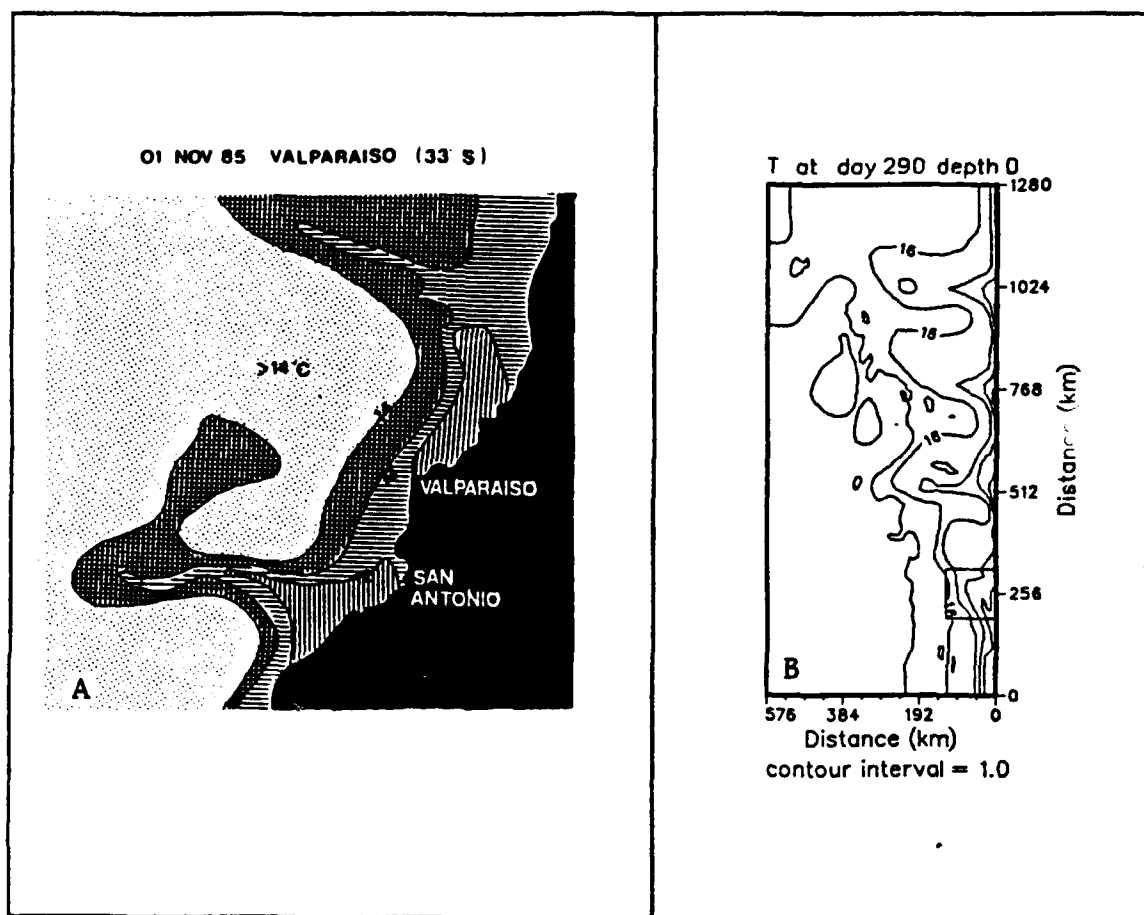


Figure 34. Temperature contours from (A) satellite and (B) model output: (A) Satellite-derived temperatures from Fonseca (1989); (B) Temperature contours from day 290 of Experiment 2. All temperatures are in °C. The inside box at $y \sim 256$ km in (B) corresponds to the size of the region shown in (A).

BIBLIOGRAPHY

- Arakawa, A., and V. R. Lamb, 1977: Computational design of the basic dynamical process of the UCLA general circulation model. *Methods in Computational Physics*, J. Chang, Ed., Academic Press, 17, 173-265.
- Bakun, A., and C. S. Nelson, 1991: The seasonal cycle of wind stress curl in subtropical eastern boundary current regions. Submitted to *J. Phys. Oceanogr.*
- Batteen, M. L., 1989: Model simulations of a coastal jet and undercurrent in the presence of eddies and jets in the California Current System. *Poleward Flows Along Eastern Ocean Boundaries*, S. J. Neshyba, C. N. K. Mooers, R. L. Smith and R. T. Barber, Eds., Springer-Verlag, 263-279.
- Batteen, M. L., and Y. -J. Han, 1981: On the computational noise of finite-difference schemes used in ocean models. *Tellus*, 33, 387-396.
- Batteen, M. L. and M. J. Rutherford, 1990: A numerical study of wind stress and thermal forcing effects on the ocean circulation off Western Australia. Submitted to *J. Phys. Oceanogr.*
- Batteen, M. L., R. W. Edson and C. S. Nelson, 1991: Effects of spatially varying winds on the central California Current System. Submitted to *J. Geophys. Res.*

- Batteen, M. L., R. L. Haney, T. A. Tielking and P. G. Renaud, 1989: A numerical study of wind forcing of eddies and jets in the California Current System. *J. Mar. Res.*, 47, 493-523.
- Clarke, A. J., 1989: Theoretical understanding of eastern ocean boundary poleward undercurrents. *Poleward Flows Along Eastern Ocean Boundaries*, S. J. Neshyba, C. N. K. Mooers, R. L. Smith and R. T. Barber, Eds., Springer-Verlag, 26-39.
- Esbensen, S. K., and Y. Kushnir, 1981: The heat budget of the global ocean: an atlas based on estimates from surface marine observations. Climatic Research Institute and Department of Atmospheric Sciences, Oregon State University. Climatic Res. Inst. Rep. 29, 27 pp.
- Fonseca, T. R., 1989: An overview of the poleward undercurrent and upwelling along the Chilean coast. *Poleward Flows Along Eastern Ocean Boundaries*, S. J. Neshyba, C. N. K. Mooers, R. L. Smith and R. T. Barber, Eds., Springer-Verlag, 203-218.
- Gunther, E. R., 1936: A report on oceanographical investigations in the Peru Coastal Current. *Discovery Rep.*, 13, 107-276.
- Haltiner, G. J., and R. T. Williams, 1980: *Numerical Prediction and Dynamic Meteorology*, 2nd Ed. John Wiley and Sons, 477 pp.
- Han, Y.-J., 1975: Numerical simulation of mesoscale eddies. Ph.D. dissertation, University of California, Los Angeles, 154 pp.

- Haney, R. L., 1974: A numerical study of the response of an idealized ocean to large-scale surface heat and momentum flux. *J. Phys. Oceanogr.*, 4, 145-167.
- Haney, R.L., 1985: Midlatitude sea surface temperature anomalies: A numerical hindcast. *J. Phys. Oceanogr.*, 15, 787-799.
- Haney, R. L., W. S. Shiver and K. H. Hunt, 1978: A dynamical-numerical study of the formation and evolution of large-scale ocean anomalies. *J. Phys. Oceanogr.*, 8, 952-969.
- Holland, W. R., and M. L. Batteen, 1986: The parameterization of subgrid-scale heat diffusion in eddy-resolved ocean circulation models. *J. Phys. Oceanogr.*, 16, 200-206.
- Johnson, D. R., 1989: Review and commentary to paper: An overview of the poleward undercurrent and upwelling along the Chilean coast by T. Fonseca. *Poleward Flows Along Eastern Ocean Boundaries*, S. J. Neshyba, C. N. K. Mooers, R. L. Smith and R. T. Barber, Eds., Springer-Verlag, 219-228.
- Levitus, S., 1982: Climatological Atlas of the World Ocean, NOAA Prof. Paper 13, U.S. Dept. of Commerce, Washington, D. C., 173 pp.
- List, R. J., 1984: Smithsonian Meteorological Tables, 6th Ed., 527 pp.
- McCreary, J. P., Jr., 1981: A linear stratified ocean model of the coastal undercurrent. *Phil. Trans. Roy. Soc., London, A* 302, 385-413.

- Nelson, C. S., 1977: Wind stress and wind stress curl over the California Current. NOAA Tech. Rep. NMFS-SSRF-714, U. S. Dept. of Commerce, 87 pp.
- Rabiner, L. R., M. R. Sambur and C. E. Schmidt, 1975: Applications of a nonlinear smoothing algorithm to speech processing. *IEEE, Trans. Acoust., Speech Signal Proc., ASSP-23*, 552-557.
- Robinson, A. R., J. A. Carton, C. N. K. Mooers, L. J. Walstad, E. F. Carter, M. M. Rienecker, J. A. Smith and W. G. Leslie, 1984: A real-time dynamical forecast of ocean synoptic/mesoscale eddies. *Nature*, 309, 781-783.
- Semtner, A. J., and Y. Mintz, 1977: Numerical simulation of the Gulf Stream and mid-ocean eddies. *J. Phys. Oceanogr.*, 7, 208-230.
- Silva, N., and T. Fonseca, 1983: Geostrophic component of the oceanic flow off northern Chile. *Conferencia Internacional Sobre Recursos Marinos del Pacifico*, P. Arana, Ed., 59-70.
- Tchernia, P., 1980: *Descriptive Regional Oceanography*, Pergamon Marine Series, Vol. 3, 253 pp.
- Weatherly, G. L., 1972: A study of the bottom boundary layer of the Florida Current. *J. Phys. Oceanogr.*, 2, 54-72.

Wooster, W. S., 1970: Eastern boundary currents in the South Pacific. *Scientific Exploration of the South Pacific*, W. S. Wooster, Ed., Natl. Acad. Sci., Washington, D. C., 60-68.

Wooster, W. S., and M. Gilmartin, 1961: The Peru-Chile Undercurrent. *J. Mar. Res.*, 19, 97-122.

Wooster, W. S., and J. L. Reid, Jr., 1963: Eastern boundary currents. *The Sea, Vol. 2*, M. N. Hill, Ed., Wiley International, 253-280.

Zeigler, J. M., W. D. Athearn and H. Small, 1957: Profiles across the Peru-Chile Trench. *Deep Sea Res.*, 4, 238-249.

INITIAL DISTRIBUTION LIST

		No. Copies
1.	Defense Technical Information Center Cameron Station Alexandria, VA 22304-6145	2
2.	Library, Code 52 Naval Postgraduate School Monterey, CA 93943-5002	2
3.	Chairman (Code OC/Co) Department of Oceanography Naval Postgraduate School Monterey, CA 93943-5000	1
4.	Chairman (Code MR/Hy) Department of Meteorology Naval Postgraduate School Monterey, CA 93943-5000	1
5.	Dr. Mary L. Batteen, (Code OC/Bv) Department of Oceanography Naval Postgraduate School Monterey, CA 93943-5000	2
6.	CDR Craig S. Nelson Department of Oceanography Naval Postgraduate School Monterey, CA 93943-5000	1
7.	Commander Naval Oceanography Command Stennis Space Center MS 39529-5000	1
8.	Commanding Officer Naval Ocean Research and Development Activity Stennis Space Center MS 39529-5004	1
9.	Commanding Officer Fleet Numerical Oceanography Center Monterey, CA 93943-5005	1
10.	Office of Naval Research (Code 420) 800 N. Quincy Street Arlington, VA 22217	1

- | | | |
|-----|---|---|
| 11. | Dr. D. Evans
Office of Naval Research (Code 1122PO)
800 N. Quincy Street
Arlington, VA 22217 | 1 |
| 12. | Director of Research Administration (Code 012)
Naval Postgraduate School
Monterey, CA 93943-5000 | 1 |
| 13. | LCDR Jeffrey L. Bacon
PCU GEORGE WASHINGTON (CVN-73)
3311 West Avenue
Newport News, VA 23007-2787 | 1 |
| 13. | LT Robert Edson (Code OC/Edson)
Department of Oceanography
Naval Postgraduate School
Monterey, CA 93943-5000 | 1 |